Physics of Fluids

Gravity currents propagating at the base of a linearly stratified ambient

Cite as: Phys. Fluids **33**, 066601 (2021); https://doi.org/10.1063/5.0051567
Submitted: 26 March 2021 . Accepted: 11 May 2021 . Published Online: 01 June 2021

Albert Dai, Yu-Lin Huang, and Yu-Min Hsieh

Physics of Fluids ARTICLE scitation.org/journal/phf

Gravity currents propagating at the base of a linearly stratified ambient

Cite as: Phys. Fluids **33**, 066601 (2021); doi: 10.1063/5.0051567
Submitted: 26 March 2021 · Accepted: 11 May 2021 ·
Published Online: 1 June 2021

Albert Dai,[a] Yu-Lin Huang, and Yu-Min Hsieh

AFFILIATIONS

Department of Engineering Science and Ocean Engineering, National Taiwan University, Taipei, Taiwan

[a]Author to whom correspondence should be addressed: hdai@ntu.edu.tw

ABSTRACT

Gravity currents produced from a full-depth lock release propagating at the base of a linearly stratified ambient are investigated by means of newly conducted three-dimensional high-resolution simulations in conjunction with corresponding two-dimensional simulations and laboratory experiments. A passive tracer is implemented in the simulations to quantitatively measure the energies associated with the current and the ambient. The density of heavy fluid within the lock is $\tilde{\rho}_C$, the density in the ambient of depth $\tilde{H}$ varies linearly from $\tilde{\rho}_b$ at the bottom to $\tilde{\rho}_0$ at the top, and the ambient has an intrinsic frequency $\tilde{N}$. Attention is focused on the initial slumping stage, during which the gravity currents propagate at a constant velocity $\tilde{V}$ and the internal Froude number is defined as $Fr = \tilde{V}/\tilde{N}\tilde{H}$. The dynamics of the subcritical gravity currents, i.e., $Fr < 1/\pi$, and the supercritical gravity currents, i.e., $Fr > 1/\pi$, are qualitatively different and are examined with the help of three-dimensional and two-dimensional high-resolution simulations. For the subcritical gravity currents, the flow is dominated by the internal wave, the Kelvin–Helmholtz vortices are inhibited, and the two-dimensional simulation agrees well with and serves as a good surrogate model for the three-dimensional simulation in the slumping stage. For the supercritical gravity currents, the Kelvin–Helmholtz vortices are pronounced and prone to breakup into three-dimensional structures in the slumping stage. On the one hand, for the supercritical gravity currents, the kinetic energy associated with the current and the potential energy associated with the ambient are accurately captured by the two-dimensional simulation. On the other hand, the transition distance for the slumping stage and dissipation rate in the system are underpredicted while the kinetic energy associated with the ambient and the potential energy associated with the current are overpredicted by the two-dimensional simulation for the supercritical gravity currents. Therefore, information derived from the two-dimensional simulation for the supercritical gravity currents must be treated with care. The high-resolution simulations in this study also complement the existing shallow-water formulation, which has been reported to agree well with the two-dimensional simulations with good physical assumptions and simple mathematical models.

I. INTRODUCTION

Gravity currents, also known as density currents, are flows driven by a density difference and occur in many natural and man-made environments. The readers are referred to Refs. 1 and 2 for a comprehensive introduction to this topic and review of examples.

In the literature, a large number of laboratory experiments and numerical simulations have been focused on the lock-exchange problem (see, for example, Refs. 3–22). In the lock-exchange problem, the heavy fluid is typically separated from a non-stratified ambient by a removable barrier in a horizontal channel with a rectangular cross section. When the barrier is withdrawn, the fluids of different densities are set into motion. This type of experiment has long served as a paradigm configuration for studying the propagation of gravity currents.

It is well known that, after a brief acceleration phase, the gravity current produced from a full-depth lock release propagates into a non-stratified ambient at a nearly constant front velocity, i.e.,

$$\tilde{V} = k\sqrt{\tilde{g}_0'\tilde{H}}, \tag{1}$$

in the slumping stage. Here, the heavy fluid has density $\tilde{\rho}_C$, the non-stratified ambient fluid has density $\tilde{\rho}_0$, the reduced gravity is $\tilde{g}_0' = \tilde{g}(\tilde{\rho}_C - \tilde{\rho}_0)/\tilde{\rho}_0$, $\tilde{H}$ is the depth of heavy fluid and ambient fluid and Ref. 23 reported that $k \approx 0.45$ for the full-depth lock-exchange flows.

The distance traveled by the gravity current during the slumping stage is also of interest in the literature. While the gravity current propagates forward in the slumping stage, a wave on the edge of the current propagates backward and reflects from the wall of the channel. Once

the reflected wave catches up with the current front, the slumping stage ends and the gravity current begins to decelerate. Reference 23 reported that, when the gravity current begins to decelerate, the current has traveled a distance $\tilde{X}_{tr} \approx 9\tilde{L}_0$ measured from the lock gate to the front of the current, where $\tilde{L}_0$ is the length of heavy fluid in the lock. For gravity currents at sufficiently large Reynolds numbers, the inertial phase follows the slumping stage and the gravity currents decelerate in time following $\tilde{V} \sim \tilde{t}^{-1/3}$.[24]

When the ambient is stratified, the dynamics between the gravity currents and the ambient may be different. Because the stratified ambient supports internal waves, which are excited by the propagation of gravity currents, the internal waves can both react to and interact with the gravity currents. Furthermore, the relative strengths of the current and the stratification in the ambient determine the layer along which the gravity current propagates. For example, when the density of heavy fluid matches the density at some intermediate level in the ambient, intrusive gravity currents are produced as considered by Refs. 25–32.

When the density of heavy fluid is greater than, or equal to, the density at the bottom of the stratified ambient, the gravity currents propagate along the lower boundary of the channel.[33–36] Reference 33 considered the propagation of a gravity current into a linearly stratified ambient using laboratory experiments and two-dimensional numerical simulations. Reference 37 extended Benjamin's classical analysis to describe the "steady-state" front velocity of a gravity current propagating into a linearly stratified ambient as a function of the stratification and agreement was found with the numerical simulations conducted by Ref. 38. Reference 36 extended the case for gravity currents propagating with constant speed into a stratified ambient with a general density profile. Solution curves in Ref. 36 have an energy-conserving upper bound, i.e., the conjugate state, which approaches Benjamin's energy-conserving solution and a lower bound which occurs when the front speed becomes critical with respect to the linear long waves generated in the ambient. In this study, our interest is in the gravity currents propagating into a linearly stratified ambient, and we summarize the conclusions in Ref. 33 as a basis of our understanding of the problem and from which we shall expand our investigation in a wider range of the strength of stratification in the ambient using high-resolution simulations and laboratory experiments. For a linearly stratified ambient, the following dimensionless stratification parameter,

$$R = \frac{\tilde{\rho}_C - \tilde{\rho}_0}{\tilde{\rho}_b - \tilde{\rho}_0}, \tag{2}$$

is introduced to give a measure of the relative strengths of the current and the stratification, where the density of heavy fluid is $\tilde{\rho}_C$, the density at the bottom of the ambient is $\tilde{\rho}_b$, and the density at the top of the ambient is $\tilde{\rho}_0$. For a gravity current propagating at the base of a linearly stratified ambient, it is required that $\tilde{\rho}_C \geq \tilde{\rho}_b$, i.e., $R \geq 1$. The "classic" case with heavy fluid propagating into a homogeneous ambient corresponds to the limit $\tilde{\rho}_b \to \tilde{\rho}_0$, i.e., $R \to \infty$. Equivalently, the relative strengths of the current and the stratification can also be defined as

$$S = \frac{\tilde{\rho}_b - \tilde{\rho}_0}{\tilde{\rho}_C - \tilde{\rho}_0}, \tag{3}$$

which is used in Refs. 36, 39, and 40. The parameter S is related to R via $S = 1/R$ and maps $R \in [1, \infty]$ to $S \in [0, 1]$. The "classic" case with heavy fluid propagating into a homogeneous ambient corresponds to $S = 0$. In a linearly stratified ambient of finite depth $\tilde{H}$, the squared intrinsic frequency is given by $\tilde{N}^2 = \tilde{g}(\tilde{\rho}_b - \tilde{\rho}_0)/\tilde{\rho}_0\tilde{H}$ and the propagating speed of the linear, mode-one, long wave is $\tilde{N}\tilde{H}/\pi$. The front velocity of current relative to that of the internal wave can be measured using the internal Froude number,

$$Fr = \frac{\tilde{V}}{\tilde{N}\tilde{H}}, \tag{4}$$

which was found to be a logarithmic function of R. In the limit of large R, i.e., $\tilde{\rho}_b \to \tilde{\rho}_0$, the stratification is weak relative to the current and the current is expected to behave like one propagating into a fluid of density $(\tilde{\rho}_b + \tilde{\rho}_0)/2$. Using the result of (1)[23] and after some algebra, the internal Froude number, in the limit of large R, approaches asymptotically to

$$Fr_{LR} = k\sqrt{R\left(1 - \frac{1}{2R}\right)} \approx kR^{1/2}, \tag{5}$$

where $k \approx 0.45$ for the gravity currents produced from a full-depth lock release. For the subcritical gravity currents, i.e., $Fr < 1/\pi$ when the internal wave travels faster than the current, the fast moving internal wave results in an oscillation of the front velocity of the current and the transition distance, $\tilde{X}_{tr}$, traveled by the slumping stage, increases with the internal Froude number. For the supercritical gravity currents, i.e., $Fr > 1/\pi$ when the current travels faster than the internal wave, the front velocity decay was monotonic and the transition distance $\tilde{X}_{tr}$ was found to be about 16 initial heights of heavy fluid irrespective of the stratification parameter or, equivalently, the internal Froude number. We should note that the above conclusions in Ref. 33 were based on the experiments in the stratification parameter range $1 < R \leq 3$ $(1/3 \leq S < 1)$. In this study, we performed experiments and simulations over $1 < R \leq 10$ $(1/10 \leq S < 1)$, and we will show that the transition distance for the supercritical gravity currents is sensitively dependent on the stratification parameter for sufficiently strong stratification in the ambient $R \lesssim 3$ $(S \gtrsim 1/3)$. For weak stratification in the ambient $3 \lesssim R \leq 10$ $(1/10 \leq S \lesssim 1/3)$, the transition distance is weakly dependent on the stratification parameter. It was reported by Ref. 33 that the internal Froude number in the slumping stage was a logarithmic function of the stratification parameter and this logarithmic relationship matches F_{LR} in the limit of large R. Later, we will also show that the internal Froude number is a logarithmic function of the stratification parameter only in the range $1 < R \lesssim 3$ $(1/3 \lesssim S < 1)$ and the logarithmic relationship and F_{LR} diverge for large R in the range $3 \lesssim R \leq 10$ $(1/10 \leq S \lesssim 1/3)$ and the prediction based on the shallow-water model appropriately describes the internal Froude number over the whole range $1 < R \leq 10$ $(1/10 \leq S < 1)$ in this study. Reference 39 investigated the problem set-forth in Ref. 33 with the shallow-water model and two-dimensional numerical simulations, using a different numerical technique. The shallow-water model, supported by two-dimensional simulations, captures well the effects of stratification when the gravity current propagates at a constant speed along the lower boundary. Reference 40 focused on the exchange of energy for a gravity current propagating along the lower boundary into a linearly stratified ambient, also with the shallow-water model and two-dimensional simulations. Good agreement on the energy of the current between the shallow-water model and the two-

dimensional simulations was found. The stratification in the ambient was found to enhance the accumulation of potential energy in the ambient and to reduce the energy decay in the system. It is also worth noting that for analytical progress a one-layer shallow-water model was developed. The major deficiency of the one-layer shallow-water model is that the motion in the ambient is omitted. A reliable two-layer shallow-water model for the problem is still lacking.

The purpose of the present investigation is to deepen our understanding of the gravity currents propagating at the base of a linearly stratified ambient by means of newly conducted three-dimensional high-resolution simulations of the Navier–Stokes equations with the Boussinesq approximation in conjunction with corresponding two-dimensional simulations and laboratory experiments. Passive tracer is implemented in the simulations to quantitatively measure the energies associated with the current and the ambient. Laboratory experiments were also conducted for comparison. In light of the results from three-dimensional high-resolution simulations and laboratory experiments, we may understand how well two-dimensional simulations perform, for both the subcritical and supercritical gravity currents and for both the energies associated with the current and the ambient. With the simulation and experimental results, previous conclusions are carefully revised and the information based on the two-dimensional simulations for the subcritical and supercritical gravity currents are evaluated. In Sec. II, we describe the formulation of the problem and the implementation of numerical methods. In Sec. III, we describe the experimental setup. The qualitative and quantitative results are presented in Sec. IV. Finally, conclusions are drawn in Sec. V.

II. FORMULATION

Figure 1 gives a sketch of the initial configuration for the gravity currents propagating into a linearly stratified ambient. The gravity currents are produced from a full-depth lock release. The height of the lock region is $\tilde{H}$, which is the same as the ambient region, and the length of the lock region is $\tilde{L}_0$. Outside the lock region is the ambient, of which the density varies linearly from $\tilde{\rho}_b$ at the bottom to $\tilde{\rho}_0$ at the top. The gravitational acceleration is in the antiparallel direction of x_3. Here, we adopt the Boussinesq approximation, in that the density difference is sufficiently small, i.e., $(\tilde{\rho}_C - \tilde{\rho}_0) \ll \tilde{\rho}_0$, so that the influence of density variations is retained only in the buoyancy term but neglected in the inertia and diffusion terms.

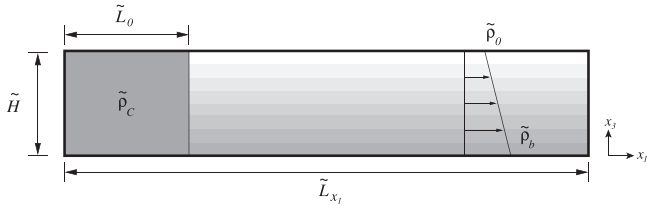

FIG. 1. Sketch of the initial condition for a gravity current produced by a full-depth lock release propagating into a linearly stratified ambient. The heavy fluid has density $\tilde{\rho}_C$, height H, and length $\tilde{L}_0$. Outside the lock is the ambient of which the density at the bottom is $\tilde{\rho}_b$ and the density at the top is $\tilde{\rho}_0$. The streamwise and wall-normal directions are represented by x_1 and x_3, respectively, while the spanwise direction x_2 is pointing into the paper. The height of the ambient is chosen the same as the height of the heavy fluid. Removal of the lock gate sets the fluids into motion.

In order to highlight the heavy fluid originally contained within the lock, here we introduce a passive tracer, namely C, for the heavy fluid originally contained within the lock region and the passive tracer follows the mass transport equation as the density field. The notion of introducing the passive tracer in the region behind the lock is identical to adding dye to the heavy fluid in the experiments. The governing equations, including the continuity, momentum, density, and tracer transport,[40] take the following tensor form:

$$\frac{\partial u_k}{\partial x_k} = 0, \tag{6}$$

$$\frac{\partial u_i}{\partial t} + u_k \frac{\partial u_i}{\partial x_k} = (\rho - \rho_a) e_i^g - \frac{\partial p}{\partial x_i} + \frac{1}{Re} \frac{\partial^2 u_i}{\partial x_k \partial x_k}, \tag{7}$$

$$\frac{\partial \rho}{\partial t} + u_k \frac{\partial \rho}{\partial x_k} = \frac{1}{ReSc} \frac{\partial^2 \rho}{\partial x_k \partial x_k}, \tag{8}$$

$$\frac{\partial C}{\partial t} + u_k \frac{\partial C}{\partial x_k} = \frac{1}{ReSc} \frac{\partial^2 C}{\partial x_k \partial x_k}. \tag{9}$$

Here, u_i denotes the velocity, ρ the density to be defined by (11), ρ_a the density field in the linearly stratified ambient defined by (13), e_i^g the unit vector in the direction of gravity, p the pressure including the hydrostatic part due to stratification in the ambient, and C represents the concentration of passive tracer, respectively. In tensor notation of (6)–(9), the unrepeated index i is known as a free index and may be any one of $i = 1, 2, 3$. The repeated index k is known as a dummy index which represents a summation over $k = 1, 2, 3$. Here, the variables without tilde are dimensionless quantities. The set of equations (6)–(9) is made dimensionless by the lock height, $\tilde{H}$, as the length scale and the buoyancy velocity,

$$\tilde{u}_b = \sqrt{\tilde{g}_0' \tilde{H}} \quad \text{with} \quad \tilde{g}_0' = \tilde{g} \frac{\tilde{\rho}_C - \tilde{\rho}_0}{\tilde{\rho}_0}, \tag{10}$$

as the velocity scale. Here, $\tilde{\rho}_C$ is the density of heavy fluid and $\tilde{\rho}_0$ is the density at the top of the ambient. The dimensionless density is given by

$$\rho = \frac{\tilde{\rho} - \tilde{\rho}_0}{\tilde{\rho}_C - \tilde{\rho}_0}. \tag{11}$$

In the ambient, the dimensionless density at the bottom is $\rho_b = (\tilde{\rho}_b - \tilde{\rho}_0)/(\tilde{\rho}_C - \tilde{\rho}_0) = 1/R$, where $\tilde{\rho}_b$ is the density at the bottom of the ambient.

Other relevant dimensionless parameters are the Reynolds number Re and the Schmidt number Sc, defined by

$$Re = \frac{\tilde{u}_b \tilde{H}}{\tilde{\nu}} \quad \text{and} \quad Sc = \frac{\tilde{\nu}}{\tilde{\kappa}}, \tag{12}$$

respectively. It is assumed that the heavy fluid and ambient fluid have identical kinematic viscosity $\tilde{\nu}$ and diffusion coefficient of density field $\tilde{\kappa}$. For saline experiments, $Sc \approx 700$; however, it has been reported by researchers (e.g., Refs. 41–43) that the influence of Schmidt number is weak as long as $Sc \approx O(1)$ or larger and setting the Schmidt number to unity is a common practice in the numerical simulations for gravity currents. Therefore, we use $Sc = 1$ in all simulations in the study.

The governing equations in the velocity-pressure formulation are solved in the three-dimensional flow domain $L_{x_1} \times L_{x_2} \times L_{x_3} = 24 \times 1.5 \times 1$, where the lock length is $L_0 = 4/3$ and $L_{x_1} = 24$ is chosen

to allow unhindered development of gravity currents and internal waves in the streamwise direction. The length in the problem is non-dimensionalized by $\tilde{H}$. The governing equations are solved using the time-splitting method,[44] in which a provisional velocity, which does not satisfy the continuity condition, is calculated in the first step, and the pressure, which is used to correct the provisional velocity in such a way that the final velocity and the pressure satisfy the complete governing equations, is calculated in the second step. Fourier expansion with periodic boundary condition is employed in the streamwise and spanwise directions, i.e., x_1 and x_2. Chebyshev expansion with Gauss–Lobatto quadrature points is employed in the wall-normal direction, i.e., x_3. At the top and bottom walls, we employ no-slip condition for the velocity field, no-flux condition for the density field, and no wall-normal gradient for the pressure field. Even a nominally free surface can act as a solid surface because the contained impurities in the fluid can cause the creation of a film on the surface.[45] The influence of a free surface was recently addressed by Ref. 46. The influence of the periodic boundary condition in the streamwise direction will not be discussed here because previous investigations have shown that the influence of boundary becomes important only when the gravity currents reach within one depth scale of the boundary.[41] Neither shall we discuss the influence of the no-slip boundary condition, since Ref. 33 indicated that computations with a slip boundary condition are not in good agreement with the experiments and previous computational investigations also adopt the no-slip boundary condition.[33,39,40]

We adopt the low-storage third-order Runge–Kutta scheme[47] for time advancement. The convection and buoyancy terms are treated explicitly, and the diffusion terms are treated implicitly with Crank–Nicolson scheme. For the convection term, divergence and convective forms are alternately used to reduce the aliasing error.[48] The pressure field satisfies the Poisson's equation and is solved in the second step (projection step) in the time-splitting method. The de-aliased pseudospectral code has been employed in Refs. 24 and 49–51 for lock-exchange flows. The initial velocity field was set with a quiescent condition in all simulations. The initial density field was prescribed unity, i.e., $\rho_C = 1$, in the lock region and

$$\rho_a(x_3) = \frac{1}{R}(1 - x_3), \tag{13}$$

in the ambient with an error-function type transition in the interface region.[52] The initial density field in the ambient varies linearly from $\rho_a = R^{-1}$ at the bottom ($x_3 = 0$) to $\rho_a = 0$ at the top ($x_3 = 1$). The specification of linear stratification for the initial density field in the ambient was straightforward and did not create additional numerical complications. The initial concentration for the passive tracer C was set as unity in the lock region and zero in the ambient, also with an error-function transition. Here, we are concerned with the gravity currents at large Reynolds numbers as in Refs. 33, 39, and 40. Based on the published reports that the influence of Reynolds number on the dynamics of gravity currents diminishes as Re increases and the influence of Reynolds number can be considered weak for $Re \gtrsim 4000$,[49,51,53] the simulations in this study were fixed at $Re = 5000$ for all cases considered. To be consistent with the resolution requirement that the grid spacing must be of the order of $O(ReSc)^{-1/2}$,[41,53] we employed the grid $N_{x_1} \times N_{x_2} \times N_{x_3} = 1320 \times 96 \times 140$ in all three-dimensional simulations. For two-dimensional simulations in the domain $L_{x_1} \times L_{x_3} = 24 \times 1$, spanwise variations were prohibited and the grid $N_{x_1} \times N_{x_3} = 1320 \times 140$ was used. The time step was chosen such that the Courant number remained less than 0.5.

III. EXPERIMENTS

In order to compare with our numerical simulations and with the published results, we also conducted experiments on gravity currents propagating into a linearly stratified ambient in a Perspex channel. The Perspex channel was manufactured with a rectangular cross-section 0.2 m wide, 0.60 m deep, and 2.5 m long with transparent sidewalls. A sketch of the experimental setup is shown in Fig. 1. During the experiments, the excess density of the fluid was created using sodium chloride. The linear stratification in the ambient was created using the double-bucket method.[54] In the double-bucket method, two identical containers are joined at the bottom, while each one holds half of the volume of ambient fluid. One container is filled with fluid of density at the top of the ambient and the other container, from which the pump is able to draw water steadily, is filled with fluid of density at the bottom of the ambient. Using the double-bucket method, the density of fluid in the container being pumped decreases linearly in time and creates the desired linearly stratified ambient. The depth of the heavy fluid and the depth of the ambient fluid were both maintained at $\tilde{H} = 9$ cm in all experiments and the lock gate was placed at a distance $\tilde{L}_0 = 12$ cm from the left wall. The top fluid boundary was in contact with two sheets of Perspex, which were separated by a thin gap to allow the withdrawal of the lock gate.

A uniform LED light board and a light-diffusing screen were placed against the back wall of the channel. A Canon 700D camera (1920 × 1080 pixel resolution at 24 frames per second) was positioned 10 m away from the front wall. The heavy fluid behind the lock was colored with 10 ml of blue dye per 1 L of solution of sodium chloride, and thin, constant-density blue dye layers were introduced at selected intermediate levels in the ambient to help visualize the internal wave field. The recorded images were exported to a PC for post-processing.

Densities of the ambient and heavy fluids were measured using a density meter with an accuracy of 10^{-3} g cm^{-3}. While the stratification parameter was varied systematically over the range $1.07 \le R \le 10$, the density of the heavy fluid was maintained at $\tilde{\rho}_C = 1.072 \pm 0.042$ g cm^{-3} and the density at the top of the ambient was maintained at $\tilde{\rho}_0 = 1.011 \pm 0.042$ g cm^{-3} in the experiments. The reduced gravity, as defined by (10), was approximately $\tilde{g}'_0 = 68.05$ cm s^{-2}. The kinematic viscosity of the sodium chloride solution was taken as $\nu = 1.1 \times 10^{-2}$ cm^2 s^{-1} and the Reynolds number in the experiments, as defined by (12), was approximately 20 000. Previously in Ref. 33, the stratification parameter in the experiments was in the range $1.075 \le R \le 3$ ($1/3 \le S \le 0.93$). In this study, we have conducted the full-depth lock-exchange experiments in a linearly stratified ambient at $R = 1.07$, 1.61, 1.82, 2, 2.5, 3.33, 4, 5, 5.88, 7.14, 8, and 10 or equivalently $S = 0.93$, 0.62, 0.55, 0.50, 0.40, 0.30, 0.25, 0.2, 0.17, 0.14, 0.13, and 0.10. For each experimental setup, at least three repeated runs were performed to ensure consistent observations. The parameters in the experiments and simulations are listed in Table I.

IV. RESULTS

A. Propagation of subcritical gravity currents, $Fr < 1/\pi$

We shall begin with the propagation of a subcritical gravity current. For convenience in comparing the three-dimensional simulations with the two-dimensional ones, we use the average in the spanwise

TABLE I. The parameters in the experiments and simulations, including the dimensionless stratification parameter R, dimensionless intrinsic frequency $N = \tilde{N}\tilde{H}\tilde{u}_b^{-1}$, internal Froude number Fr, dimensionless transition distance X_{tr}, and transition time multiplied by the intrinsic frequency NT_{tr}.

Exp./Sim.	R	N	Fr	X_{tr}	NT_{tr}
Exp.	1.07	0.967	0.265	11.28	43.79
Exp.	1.61	0.788	0.434	15.75	40.94
Exp.	1.82	0.741	0.481	14.90	35.50
Exp.	2.00	0.707	0.533	13.79	28.37
Exp.	2.50	0.632	0.599	13.61	24.53
Exp.	3.33	0.548	0.735	13.45	19.89
Exp.	4.00	0.500	0.800	13.01	17.75
Exp.	5.00	0.447	0.944	12.99	14.76
Exp.	5.88	0.412	1.035	12.65	14.76
Exp.	7.14	0.374	1.143	12.31	11.43
Exp.	8.00	0.354	1.262	12.26	10.51
Exp.	10.00	0.316	1.449	12.13	9.40
Sim. (2D)	1.02	0.990	0.260	10.31	40.54
Sim. (2D)	1.07	0.967	0.293	11.51	43.34
Sim. (2D)	1.12	0.945	0.307	12.44	44.37
Sim. (2D)	1.20	0.913	0.314	14.94	45.70
Sim. (2D)	1.30	0.877	0.339	14.13	40.00
Sim. (2D)	1.40	0.845	0.362	13.75	36.69
Sim. (2D)	1.50	0.816	0.386	13.61	34.35
Sim. (2D)	1.60	0.790	0.467	13.49	32.37
Sim. (2D)	2.00	0.707	0.545	9.95	21.70
Sim. (2D)	3.00	0.577	0.719	10.18	16.94
Sim. (2D)	4.00	0.500	0.852	9.73	14.07
Sim. (2D)	5.00	0.447	0.997	9.98	12.30
Sim. (2D)	7.00	0.378	1.186	9.69	9.84
Sim. (2D)	10.00	0.316	1.455	9.60	8.03
Sim. (3D)	1.07	0.967	0.301	11.28	42.38
Sim. (3D)	1.60	0.790	0.467	15.75	41.03
Sim. (3D)	2.00	0.707	0.545	13.79	30.55
Sim. (3D)	5.00	0.447	0.997	12.99	15.18
Sim. (3D)	10.00	0.316	1.455	12.31	10.06

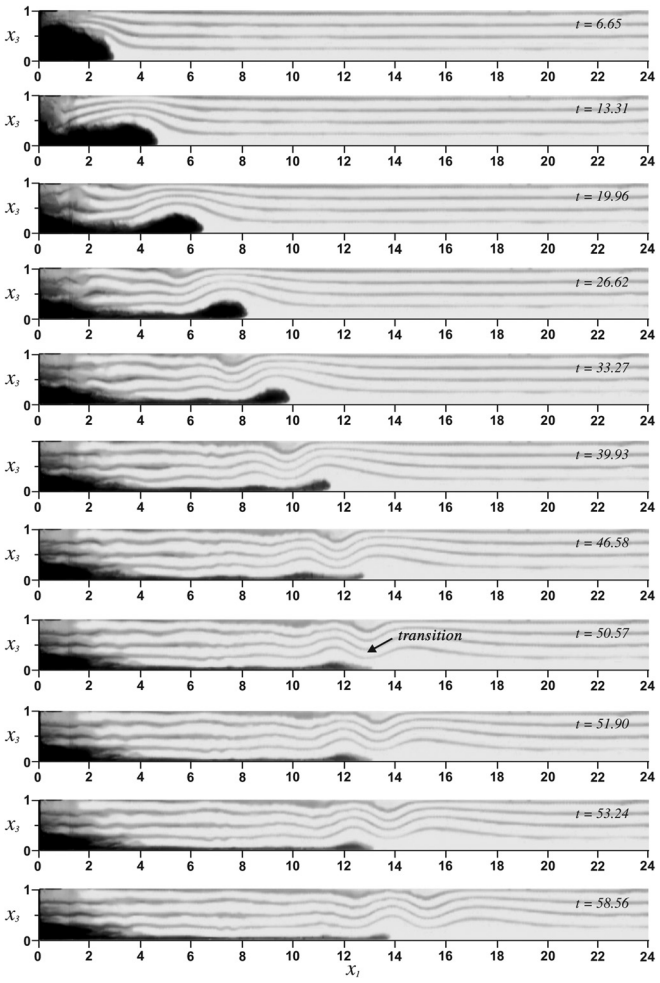

FIG. 2. Sequence of images showing a subcritical gravity current in the experiment. In this case, the stratification parameter is $R = 1.07$ and the internal Froude number is $Fr = 0.27$. Distances in the vertical and horizontal directions are normalized by the depth of flow $\tilde{H}$, and the scale is exaggerated in the vertical direction. The black lines in the ambient represent the isopycnals. Dimensionless time instances are chosen at t = 6.65, 13.31, 19.96, 26.62, 33.27, 39.93, 46.58, 50.57, 51.90, 53.24, and 58.56.

direction for dimensionless density $\rho(x_1, x_2, x_3)$ and the concentration of the passive tracer $C(x_1, x_2, x_3)$ in three-dimensional simulations. The average of a variable $f(x_1, x_2, x_3)$ in the spanwise direction is defined as

$$\bar{f}(x_1, x_3) = \frac{1}{L_{x_2}} \int_0^{L_{x_2}} f(x_1, x_2, x_3) dx_2, \tag{14}$$

where the variable f can be the dimensionless density ρ and the concentration of the passive tracer C and $L_{x_2} = 1.5$ is chosen in the three-dimensional simulations.

For subcritical gravity currents, we conducted two-dimensional simulations for full-depth lock-exchange in a linearly stratified ambient at $R = 1.02$, 1.07, and 1.12 and three-dimensional simulations at $R = 1.07$. Figure 2 shows a time sequence of images from an experiment of a subcritical gravity current propagating into a linearly stratified ambient at $R = 1.07$, where the black lines in the ambient represent the isopycnals. This case is a typical example of gravity currents propagating at a speed less than that of the linear, mode-one internal wave. As the gravity current moves forward, a second wave begins to form behind the first wave, as shown in Fig. 2 at $t = 33.27$. The current interacts with the second wave and, as a result, a second elevation of the dyed fluid appears following the current front at $t = 39.93$. Since the internal wave moves faster than the gravity current, the wave trough following the first wave crest catches up with the current front at $t = 50.57$ and eventually stops and outruns the current front at $t = 53.24$, 58.56.

Figure 3 shows the passive tracer for the gravity current and the dimensionless density in the ambient of a subcritical gravity current

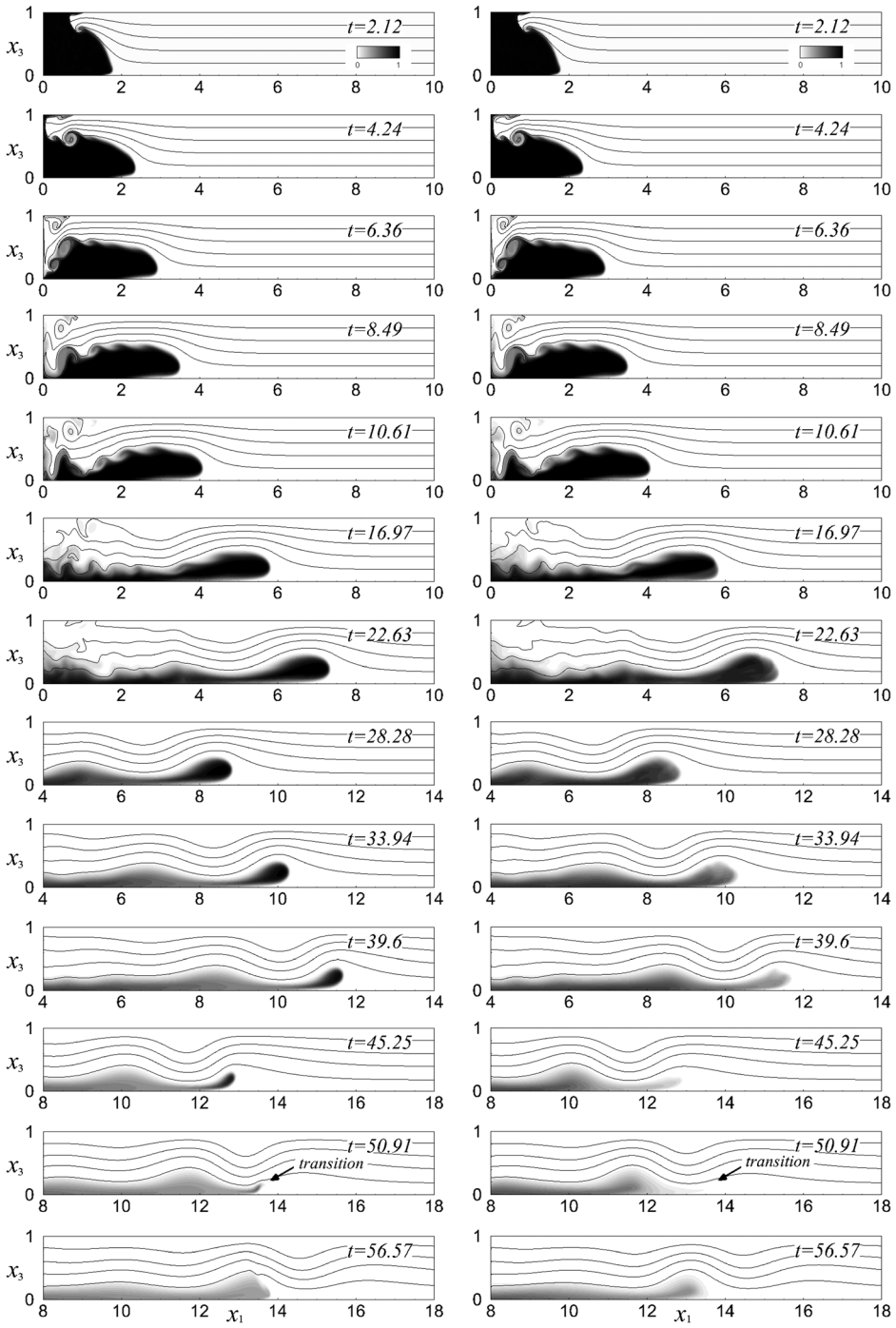

FIG. 3. Sequences of images of a subcritical gravity current in the two-dimensional simulation (left column) and three-dimensional simulation (right column). In this case, the stratification parameter is $R = 1.07$ and the internal Froude number is $Fr = 0.30$. The black lines in the ambient represent the isopycnals. Time instances are chosen at (top-bottom) $t = 2.12$, 4.24, 6.36, 8.49, 10.61, 16.97, 22.63, 28.28, 33.94, 39.60, 45.25, 50.91, and 56.57 dimensionless units for both the two-dimensional and three-dimensional simulations.

with $R = 1.07$ based on two-dimensional (left column) and three-dimensional (right column) simulations. Here, the spanwise-averaged concentration of the passive tracer $\bar{C}$ and dimensionless density $\bar{\rho}$ are shown for the three-dimensional simulation. It is observed that both the two-dimensional and three-dimensional simulations yield consistent results and capture the interactions between the internal wave and current described above. We should note that under the influence of the internal wave, the body of the subcritical gravity current maintains a smooth, curved shape without strong mixing with the ambient fluid, as shown by both two-dimensional and three-

dimensional simulations in Fig. 3 at $t = 16.97$, 22.63, 28.28, and 33.94. While the lobes and clefts must be missing in two-dimensional simulation, they do appear in three-dimensional simulation during $15 < t < 40$. Since the average in the spanwise direction cannot display the three-dimensional structure of the lobes and clefts, here we show a three-dimensional view of the isosurface of the passive tracer concentration at $t = 22.63$ in Fig. 4. Otherwise, there is only a slight difference between the two-dimensional and three-dimensional simulations in the passive tracer field at $t = 39.60$ and 45.25 when the internal wave trough following the first wave crest catches up with the current front. We will show later that such a slight difference has negligible influence on the energy balances.

Figure 5 shows the front position vs time for the subcritical gravity current at $R = 1.07$ as described above. After released from the lock, the subcritical gravity current propagates forward approximately at a constant speed $V \approx 0.29$ until $t \approx 50$, when the wave trough following the first wave crest passes through the current front. We should note that the two-dimensional and three-dimensional simulations agree nicely with the experimental results for the subcritical gravity current. During the slumping stage of the subcritical gravity current at $R = 1.07$, for which the internal wave moves faster than the current, the internal Froude number $Fr \approx 0.30$ is less than $1/\pi$. In the experiments and simulations, the internal Froude number is calculated based on (4), namely, the ratio of the gravity current speed in the slumping phase (V) to the internal wave speed (NH). Based on Fig. 5, we may further define the transition distance X_{tr} and time T_{tr} traveled by the slumping stage as the front velocity, namely the local slope of x vs t, falls to 80% of the slumping velocity. As long as this criterion is consistently applied in selecting the transition distance and time, it is possible to quantitatively measure the dependence of transition distance and time on other parameters in the slumping stage, e.g., the internal Froude number. For the subcritical gravity currents, the internal Froude number and the transition distance and time are captured by the two-dimensional simulation, which agrees well with the three-dimensional simulation and the experiment.

B. Propagation of supercritical gravity currents, $Fr > \frac{1}{\pi}$

For a supercritical gravity current, the current moves faster than the internal wave. For supercritical gravity currents, we conducted

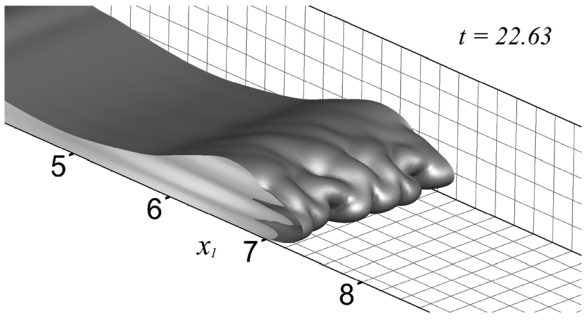

FIG. 4. Three-dimensional view of the lobes and clefts for the subcritical gravity current at $R = 1.07$ and the internal Froude number is $Fr = 0.30$. The gravity current front is visualized by an isosurface of the passive tracer concentration $C = 0.25$. Time instance is chosen at $t = 22.63$ dimensionless units.

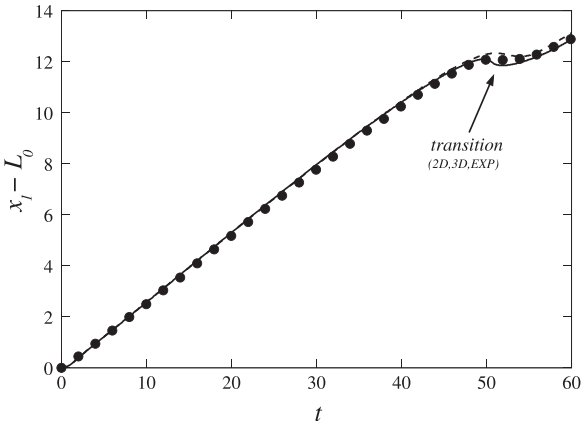

FIG. 5. The front position, $x - L_0$, vs time, t, for a subcritical gravity current. The front position and time are non-dimensionalized by $\tilde{H}$ and $\tilde{H}\tilde{u}_b^{-1}$, respectively. In this case, the stratification parameter is $R = 1.07$ and the internal Froude number is $Fr = 0.30$. Symbol: ●, present experiment. The solid line represents the three-dimensional simulation, and the dashed line represents the two-dimensional simulation in this study.

two-dimensional simulations for full-depth lock-exchange in a linearly stratified ambient at $R = 1.6$, 2, 3, 4, 5, 7, and 10 and three-dimensional simulations at $R = 1.6$, 2, 5, and 10. Figure 6 shows a time sequence of images from an experiment of a supercritical gravity current propagating into a linearly stratified ambient at $R = 2$, where the black lines in the ambient represent the isopycnals. This case is a typical example of supercritical gravity currents. As the gravity current moves forward, the head of the current and the wave crest are locked together, and there is no strong evidence for a second wave following the first wave during the slumping stage.

Figure 7 shows the passive tracer and the dimensionless density in the ambient of a supercritical gravity current at $R = 2$ based on two-dimensional (left column) and three-dimensional (right column) simulations, where the spanwise-averaged concentration of the passive tracer $\bar{C}$ and dimensionless density $\bar{\rho}$ are shown for the three-dimensional simulation. It is observed that both the two-dimensional and three-dimensional simulations yield consistent results up to $t \approx 18.38$, as shown in Fig. 7. The Kelvin–Helmholtz vortices are persistent during the slumping stage in the two-dimensional simulation, as shown in Fig. 7 (left column), while these vortices are also pronounced in the three-dimensional simulation but are allowed to breakup into three-dimensional structures, as shown in Fig. 7 (right column). We note that the three-dimensional simulation shows consistent behaviors as in the experiment, as shown in Fig. 6. It is also worth noting that in the three-dimensional simulation, the supercritical gravity current moves faster than the counterpart in the two-dimensional simulation, as shown in Fig. 7 at $t = 39.60$, 45.25, and 50.91.

Figure 8 shows the front position vs time for the supercritical gravity current at $R = 2$ as described above. During the slumping stage, the supercritical gravity current propagates forward approximately at a constant speed $V \approx 0.38$ and the internal Froude number $Fr \approx 0.54$ is greater than $1/\pi$. We note that the experiment, two-dimensional and three-dimensional simulations all give consistent results on the

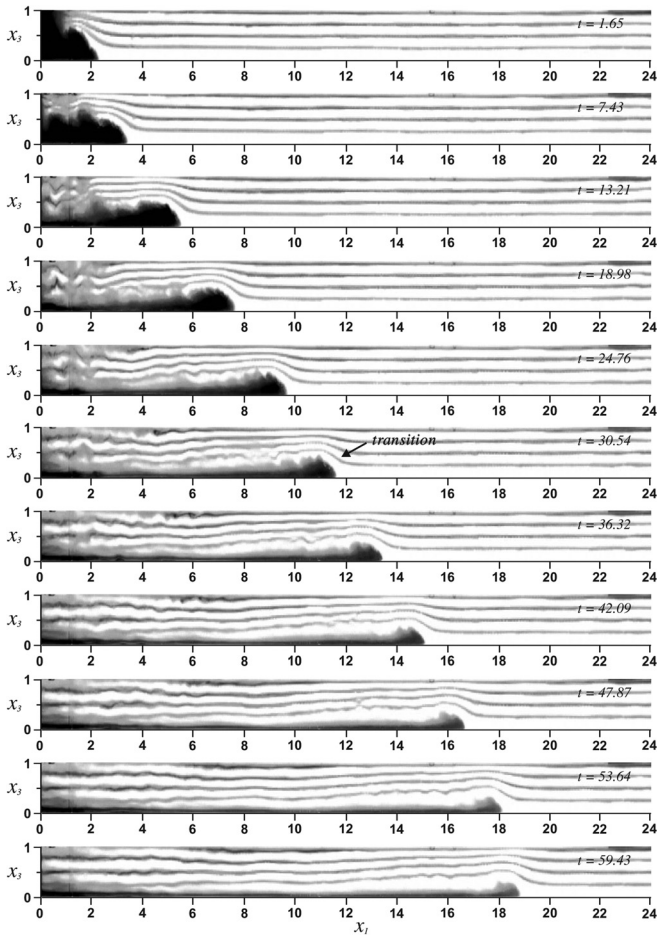

FIG. 6. Sequence of images showing a supercritical gravity current in the experiment. In this case, the stratification parameter is $R = 2$ and the internal Froude number is $Fr = 0.53$. Distances in the vertical and horizontal directions are normalized by the depth of flow $\tilde{H}$, and the scale is exaggerated in the vertical direction. The black lines in the ambient represent the isopycnals. Dimensionless time instances are chosen at $t = 1.65$, 7.43, 13.21, 18.98, 24.76, 30.54, 36.32, 42.09, 47.87, 53.64, and 59.43.

front speed of the supercritical gravity current. However, the slumping stage for the supercritical gravity current lasts significantly farther in the experiment and three-dimensional simulation than in the two-dimensional simulation.

Previously, it was reported by Ref. 33 that the internal Froude number is a logarithmic function of the stratification parameter, i.e., $Fr = 0.266 + 0.912\log(R)$ for the full-depth release case, and the logarithmic relationship matches F_{LR}, as defined by (5), in the limit of large R, cf. Fig. 11 in Refs. 33–39 pointed out that the logarithmic relationship is a good approximation for the prediction based on the shallow-water model but speculated that the logarithmic relationship might fail outside $1 \le R \le 10/3$ $(0.3 \le S \le 1)$. Figure 9 shows the internal Froude number vs the stratification parameter on a semi-logarithmic plot in the range $1 < R \le 10$ in this study. As expected, in the range $1 < R \lesssim 3$, the internal Froude number follows the logarithmic relationship proposed by Ref. 33 for the full-depth release case. However, in the range $3 \lesssim R \le 10$, the internal Froude number apparently follows the asymptote Fr_{LR}, given in Eq. (5), in the limit of large R rather than the logarithmic relationship. As the stratification in the ambient becomes relatively weak, indeed, it is expected that the internal Froude number approaches the asymptote Fr_{LR} in the limit of large R, but here we confirm the speculation that the logarithmic relationship fails outside the range $1 < R \lesssim 3$ and the previous perception that the logarithmic relationship matches the asymptote Fr_{LR} in the limit of large R has to be revised. Figure 9 also shows that the prediction based on the shallow-water model[2,39] appropriately describes the internal Froude number based on our simulations and experiments over the whole range $1 < R \le 10$ in this study.

Figure 10 shows the transition distance (X_{tr}) as a function of the internal Froude number. Here, the transition distance is non-dimensionalized by the depth of the heavy fluid, $\tilde{H}$. Figure 11 shows the transition time (T_{tr}) multiplied by the intrinsic frequency (N) into a group, NT_{tr}, as a function of the internal Froude number. Here, the transition time is multiplied by the intrinsic frequency, i.e., NT_{tr}, to be consistent and compared with Ref. 33. Since the depth of heavy fluid is fixed in our problem setup, X_{tr} and NT_{tr} can be functions of the independent variable R and the dependent variable Fr. As we have shown, Fr is a one-to-one function of R and we may choose to plot X_{tr} and NT_{tr} vs Fr to make a comparison with Ref. 33. In order to show the experimental data trend, the results based on the partial-depth lock release reported by Ref. 33 are also included for reference.

It is clear based on Figs. 10 and 11 that the dynamics between the subcritical gravity currents, i.e., $Fr < 1/\pi$, and the supercritical gravity currents, i.e., $Fr > 1/\pi$, are qualitatively different. For the subcritical gravity currents, the internal wave dominates the propagation of gravity currents and the termination of the slumping stage is caused by the wave trough following the first wave crest overrunning the current front. For the subcritical gravity currents, both X_{tr} and NT_{tr} increase as Fr increases, because the difference between the internal wave and the current speeds decreases as Fr increases toward $1/\pi$. For the supercritical gravity currents, the current front and the primary wave are locked together and the primary wave removes energy from the current. We note, in particular, for the supercritical gravity currents both X_{tr} and NT_{tr} decrease as the internal Froude number (or equivalently the stratification parameter) increases. A possible physical explanation is that, as the internal Froude number (or the stratification parameter) increases, the internal wave in the ambient becomes slower such that the speed difference between the gravity current and the internal wave increases. The gravity current in this situation is less likely to be held by the internal wave for extended distance and time in the slumping phase. While it was concluded by Ref. 33 that the transition distance was constant (16 initial heights of heavy fluid) for all the supercritical gravity currents, here we show that the transition distance is sensitively dependent on the internal Froude number for the supercritical gravity currents in the range $R \lesssim 3$ $(S \gtrsim 1/3)$ or $Fr \lesssim 0.72$. For weaker stratification in the ambient in the range $3 \lesssim R \le 10$ $(1/10 \le S \lesssim 1/3)$ or $0.72 \lesssim Fr \le 1.45$, the transition distance is weakly dependent on the internal Froude number. Such an observation suggests that stronger stratification in the ambient tends to hold the supercritical gravity currents in the slumping stage for a longer distance. In the limit of large R, i.e., $S \to 0$, the problem under investigation approaches the classic lock-exchange experiment with a homogeneous heavy fluid

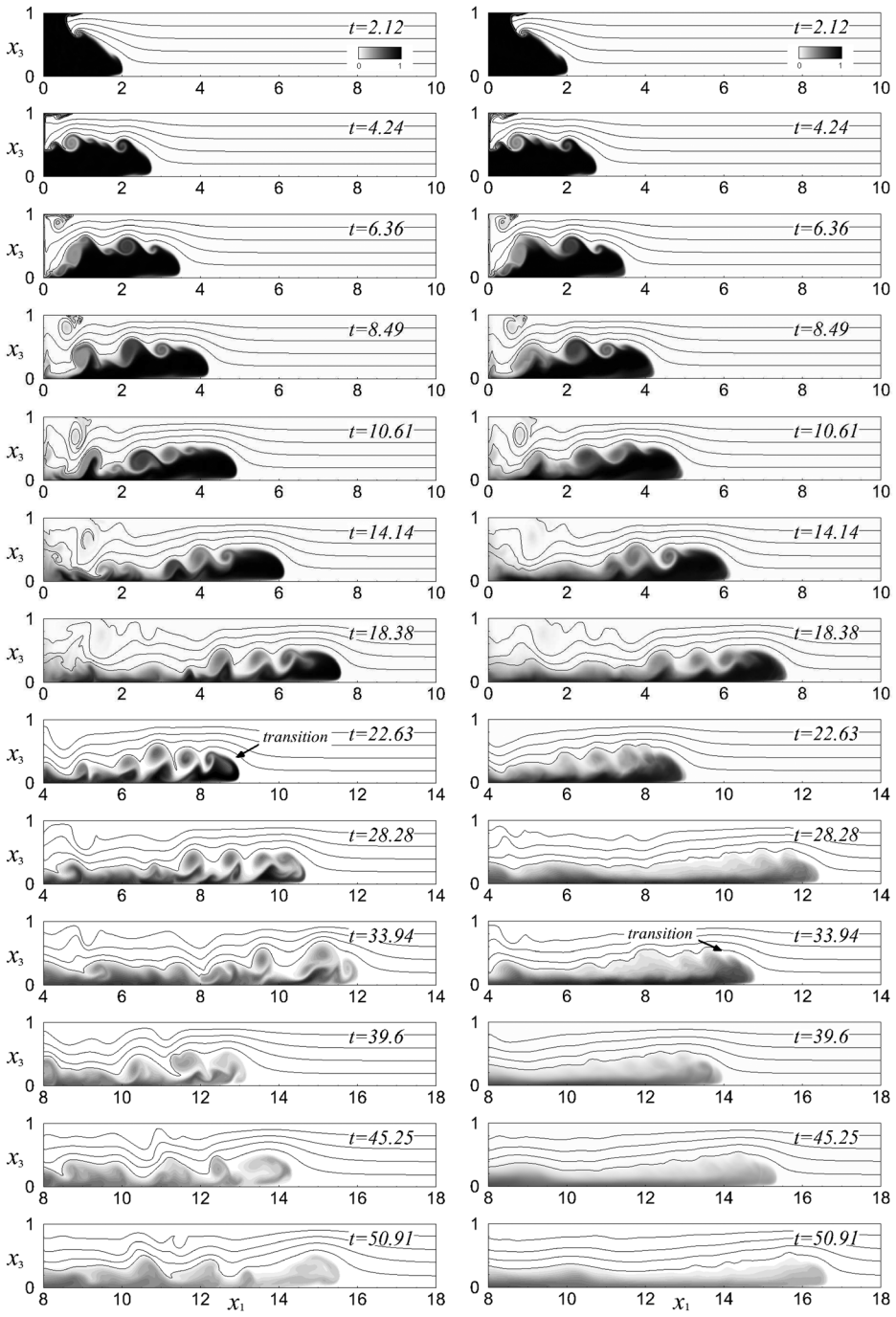

FIG. 7. Sequences of images of a supercritical gravity current in the two-dimensional simulation (left column) and three-dimensional simulation (right column). In this case, the stratification parameter is $R = 2$ and the internal Froude number is $Fr = 0.54$. The black lines in the ambient represent the isopycnals. Time instances are chosen at (top-bottom) $t = 2.12$, 4.24, 6.36, 8.49, 10.61, 14.14, 18.38, 22.63, 28.28, 33.94, 39.60, 45.25, and 50.91 dimensionless units for both the two-dimensional and three-dimensional simulations.

propagating into a homogeneous ambient. Our experiment shows that when $R = 10$ $(S = 1/10)$ or $Fr = 1.45$, the transition distance is $X_{tr} = 12.13$, which is consistent with Ref. 23 which indicated that in the classic full-depth lock-exchange experiment $X_{tr} \approx 9L_0 = 12$, where $L_0 = 4/3$ in our experimental and computational setup. Figure 10 also reveals the fact that, for the supercritical gravity currents, the transition distance is underpredicted by the two-dimensional simulations in light of the results from laboratory experiments and three-dimensional simulations. We should keep in mind that, as remarked by Ref. 39, the available one-layer shallow-water model significantly

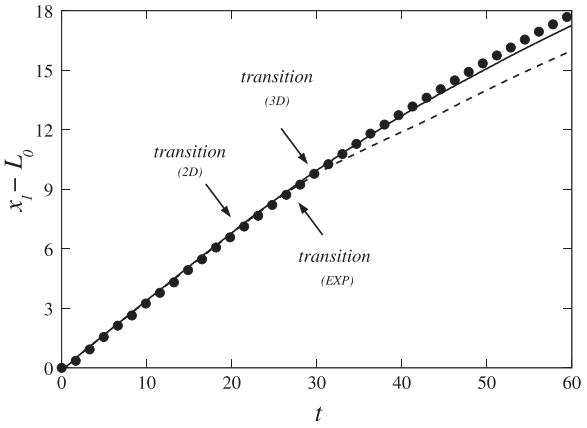

FIG. 8. The front position, $x - L_0$, vs time, t, for a supercritical gravity current. The front position and time are non-dimensionalized by $\tilde{H}$ and $\tilde{H}\tilde{u}_b^{-1}$, respectively. In this case, the stratification parameter is $R = 2$ and the internal Froude number is $Fr = 0.54$. Symbol: ●, present experiment. The solid line represents the three-dimensional simulation and the dashed line represents the two-dimensional simulation in this study.

underpredicts the transition distance for the gravity currents in a homogeneous and in a linearly stratified ambient and cannot predict well the transition distance for the full-depth lock release.

C. Energy budgets

From the point of view of energy budgets, the propagation of gravity currents into a linearly stratified ambient is a process in which the potential energy, subject to the action of stratification, is converted into kinetic energy and subsequently into dissipation by viscous friction. Such an energy conversion is similar to the process observed for gravity currents propagating into a homogeneous environment.[49–51]

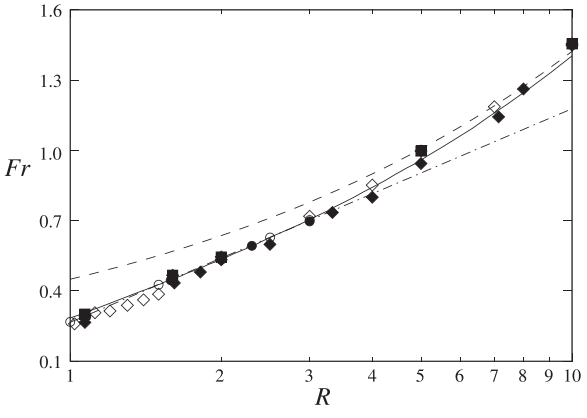

FIG. 9. Internal Froude number, Fr, vs the stratification parameter, $R = 1/S$, for the experiments and numerical simulations. Symbols: ●, experiments in Ref. 33; ○, two-dimensional simulations in Ref. 33; ◆, present experiments; ■, three-dimensional simulations in this study; ◇, two-dimensional simulations in this study. The dash-dotted line $(-.-)$ represents the logarithmic function $Fr = 0.266 + 0.912\log(R)$. The dashed line (- -) represents the asymptote $Fr_{LR} = kR^{1/2}$ in the limit of large R, where $k \approx 0.45$ for the full-depth release case. The solid line represents the prediction based on the shallow-water model.[39]

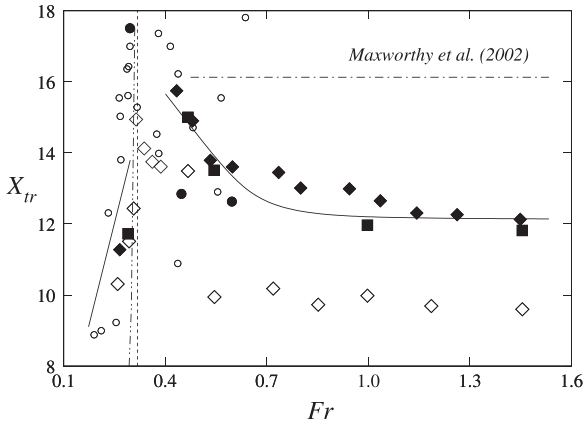

FIG. 10. The dimensionless transition distance, X_{tr}, vs the internal Froude number, Fr, for the experiments and numerical simulations. The transition distance is non-dimensionalized by $\tilde{H}$. Symbols: ●, experiments in Ref. 33 for the full-depth release; ○, experiments in Ref. 33 for the partial-depth release (non-dimensionalized by h_0, the depth of heavy fluid); ◆, present experiments; ■, three-dimensional simulations in this study; ◇, two-dimensional simulations in this study. Here, the vertical dashed line is $Fr = 1/\pi$ and the solid lines are added as a visual guide to show the data trend. The dash dotted line $(-.-)$ represents the prediction of Ref. 33 for the supercritical gravity currents and the dash double dotted line $(-..-)$ represents the prediction of Ref. 2 for the subcritical gravity currents.

However, the stratification in the ambient not only creates a greater buoyancy force that hinders the propagation of gravity currents but also supports internal waves that can receive energy from the gravity currents and transport it away. It is our understanding that information on the energy budgets can be difficult to attain in the experiments and the previously published report on the energy budgets in the problem was based on the shallow-water model and two-dimensional simulations. A particular contribution in this study is that we will provide

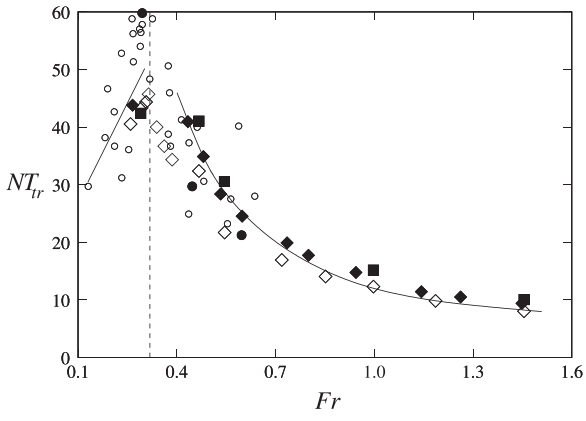

FIG. 11. The transition time multiplied by the intrinsic frequency, NT_{tr}, vs the internal Froude number, Fr, for the experiments and numerical simulations. Symbols: ●, experiments in Ref. 33 for the full-depth release; ○, experiments in Ref. 33 for the partial-depth release; ◆, present experiments; ■, three-dimensional simulations in this study; ◇, two-dimensional simulations in this study. Here, the vertical dashed line is $Fr = 1/\pi$ and the solid lines are added as a visual guide to show the data trend.

and compare the energy budgets based on the two-dimensional and three-dimensional simulations for the subcritical and supercritical gravity currents propagating into a linearly stratified ambient. We will also show that the two-dimensional simulation serves as a good surrogate model for the three-dimensional simulation for the subcritical gravity currents but may not do so for the supercritical gravity currents.

The equation for the time derivative of the kinetic energy is obtained by multiplying the momentum equation (7) by u_i, i.e.,

$$\frac{D}{Dt}\left(\frac{1}{2}u_iu_i\right) = -\frac{\partial}{\partial x_i}(pu_i) + \frac{2}{Re}\frac{\partial}{\partial x_j}(s_{ij}u_i) - \frac{2}{Re}s_{ij}s_{ij} - (\rho-\rho_a)u_3, \tag{15}$$

where D/Dt denotes the material derivative, s_{ij} denotes the strain rate tensor, $s_{ij} = \frac{1}{2}(u_{i,j} + u_{j,i})$, and u_3 denotes the velocity component in x_3 direction.[40,49–51,53] Integration of (15) over the entire flow domain $\mathscr{V}$ leads to the evolution equation of the total kinetic energy K, after rearrangement,

$$\frac{dK}{dt} + \int_{\mathscr{V}}(\rho-\rho_a)u_3dV + \frac{2}{Re}\int_{\mathscr{V}}s_{ij}s_{ij}dV = 0, \quad \text{where} \quad K(t) = \int_{\mathscr{V}}\frac{1}{2}u_iu_idV, \tag{16}$$

and the divergence terms on the right-hand side of (15) vanish upon integration. Here, we define the potential energy in the system, after subtracting the background stratification in the ambient, as

$$P(t) = \int_{\mathscr{V}}(\rho-\rho_a)x_3dV. \tag{17}$$

The vertical buoyancy flux Φ, which is the second term on the left-hand side of (16), is related to the potential energy in the system via

$$\Phi = \int_{\mathscr{V}}(\rho-\rho_a)u_3dV = \frac{d(P-I)}{dt}, \tag{18}$$

where

$$I(t) = \int_0^t \Psi(\tau)d\tau, \quad \Psi = \int_{\mathscr{V}}\frac{D(\rho-\rho_a)}{Dt}x_3dV, \tag{19}$$

represent the conversion from internal energy to potential energy and its time rate of change due to irreversible diffusion of density.[51,55] When there is no diffusion of density, the potential energy in the system can increase or decrease only via vertical buoyancy flux. When the diffusion of density is at work, the potential energy in the system increases as time progresses, i.e., $\Psi > 0$, even without the vertical buoyancy flux. The diffusion of density provides an alternative route for potential energy increase in the system but our results show that the internal energy caused by diffusion of density tends to mask the potential energy change due to vertical buoyancy flux. The third term on the left-hand side of (16) represents the dissipation rate, and we use W to denote the time integral of dissipation rate, i.e.,

$$W(t) = \int_0^t \epsilon(\tau)d\tau, \quad \epsilon = \frac{2}{Re}\int_{\mathscr{V}}s_{ij}s_{ij}dV. \tag{20}$$

Using (18) and (20), Eq. (16) is a statement of energy balance, i.e., that $K + (P-I) + W$ is a constant during the propagation of gravity currents and internal waves.

With the help of the concentration of the passive tracer, we may quantitatively measure the energies associated with the current and the ambient. Here, we use the passive tracer to decompose the energies into two parts, i.e., one associated with the gravity currents (denoted by subscript C) and the other associated with the ambient (denoted by subscript A), while the energies without subscript C or A represent those in the whole system. For example, the kinetic energy K in the system can be decomposed into

$$K_C = \int_{\mathscr{V}}\frac{1}{2}Cu_iu_idV \quad \text{and} \quad K_A = \int_{\mathscr{V}}\frac{1}{2}(1-C)u_iu_idV, \tag{21}$$

respectively. The potential energy P in the system can be decomposed into

$$P_C = \int_{\mathscr{V}}C(\rho_C-\rho_a)x_3dV \quad \text{and} \quad P_A = \int_{\mathscr{V}}(1-C)\left(\rho_a^*-\rho_a\right)x_3dV, \tag{22}$$

based on the assumption that the density field is related to the concentration of the passive tracer via $\rho = C\rho_C + (1-C)\rho_a^*$, where the dimensionless density of the initial heavy fluid is taken as $\rho_C = 1$ and ρ_a^* is the density contribution from the ambient fluid under the influence of internal waves. Other quantities such as the vertical buoyancy flux, dissipation rate and irreversible conversion of internal energy can be decomposed similarly into one associated with the current and the other associated with the ambient.

The energy budgets are normalized with the initial potential energy in the system, i.e., $P(0)$, and the superscript "n" denotes normalized contributions. The overall energy in the system $K^n + (P^n - I^n) + W^n$ during the simulations is observed to be conserved to a very high degree of accuracy. Because the irreversible diffusion of density masks the potential energy change due to vertical buoyancy flux, here we show the potential energy with internal energy subtracted as $(P^n - I^n)$. Figure 12 shows the energy budget for the subcritical gravity current propagating into a linearly stratified ambient at $R = 1.07$ ($S \approx 0.93$). For the subcritical case, the potential energy decays monotonically while the kinetic energy increases initially, with a maximum of $K^n \approx 0.22$ at $t \approx 4.74$, and decreases afterward. The kinetic energy reaches its maximum before the end of the slumping stage, which occurs at $T_{tr} \approx 40$ (44) based on the three-dimensional (two-dimensional) simulations for the subcritical gravity current at $R = 1.07$ ($S \approx 0.93$). More importantly, the energy budgets based on the two-dimensional and three-dimensional simulations agree nicely for the subcritical case throughout the slumping stage. Consistent with the shallow-water model reported by Ref. 40, it is interesting to note that the interaction between the internal wave and gravity current at $t \approx 50$ leaves no detectable footprints in the energy exchange as shown in Fig. 12. Figure 13 shows the energy components associated with the current and the ambient. It may be concluded that the two-dimensional and three-dimensional

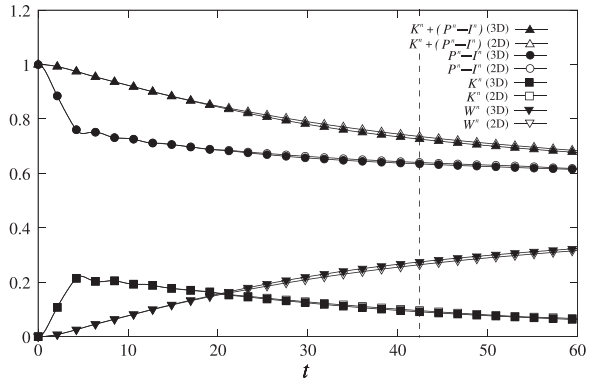

FIG. 12. Energy budget in the system for a subcritical gravity current at $R = 1.07$ ($S \approx 0.93$). Symbols: ▲, total mechanical energy $K^n + (P^n - I^n)$ (3D); △, total mechanical energy (2D); ●, potential energy $(P^n - I^n)$ (3D); ○, potential energy (2D); ■, kinetic energy K^n (3D); □, kinetic energy (2D); ▼, dissipated energy W^n (3D); ▽, dissipated energy (2D). Dashed line represents the transition time based on the 3D simulation.

simulations agree well in almost all energy components for the subcritical case except for the dissipation rate associated with the current at $15 < t < 40$. Three-dimensional simulation shows that lobes and clefts, which must be missing in the two-dimensional simulation, take shape during $15 < t < 40$ and therefore the dissipation rate in the three-dimensional simulation differs from that in the two-dimensional simulation. Nevertheless, the lobes and clefts are inhibited by the internal wave for the subcritical case and the difference in the dissipation rate between the two-dimensional and three-dimensional simulations diminishes when the wave trough catches up with the front, as shown in Fig. 13(c). The vertical buoyancy flux associated with the ambient, Φ_A^n, is positive for $0 \leq t \lesssim 20$, during which the stratified ambient accumulates potential energy in the ambient. For $t \gtrsim 20$, Φ_A^n is negative but close to zero which indicates that the potential energy in the ambient slightly decreases, as shown in Figs. 13(b) and 13(d). The vertical buoyancy flux associated with the current, Φ_C^n, is negative throughout the propagation, which indicates that the potential energy in the current monotonically decreases during the slumping stage, as also shown in Figs. 13(b) and 13(d).

Figure 14 shows the energy budget for the supercritical gravity current propagating into a linearly stratified ambient at $R = 2$ ($S = 0.5$). For the supercritical case at $R = 2$ ($S = 0.5$), the potential energy also decays monotonically while the kinetic energy reaches its maximum of $K^n \approx 0.34$ at $t \approx 4.45$ before the end of the slumping stage at $T_{tr} \approx 43$ (31) based on the three-dimensional (two-dimensional) simulations. We note that the two-dimensional and three-dimensional simulations show similar behaviors but the agreement

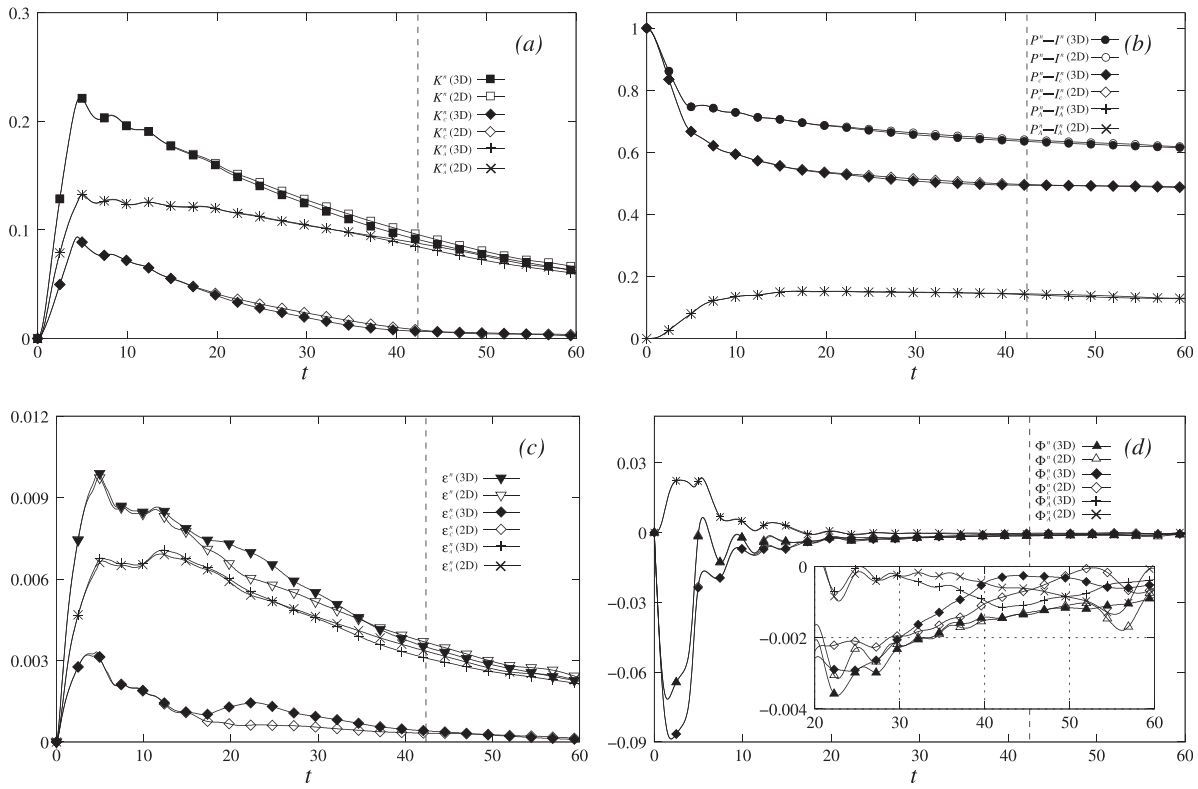

FIG. 13. Energy components in the system for a subcritical gravity current at $R = 1.07$ ($S \approx 0.93$). Panel (a) shows K^n (■, 3D; □, 2D), K_C^n (◆, 3D; ◇, 2D), K_A^n (+, 3D; ×, 2D); panel (b) shows $(P^n - I^n)$ (●, 3D; ○, 2D), $(P_C^n - I_C^n)$ (◆, 3D; ◇, 2D), $(P_A^n - I_A^n)$ (+, 3D; ×, 2D); panel (c) shows $\epsilon^n = dW^n/dt$ (▼, 3D; ▽, 2D), $\epsilon_C^n = dW_C^n/dt$ (◆, 3D; ◇, 2D), $\epsilon_A^n = dW_A^n/dt$ (+, 3D; ×, 2D); panel (d) shows $\Phi^n = d(P^n - I^n)/dt$ (▲, 3D; △, 2D), $\Phi_C^n = d(P_C^n - I_C^n)/dt$ (◆, 3D; ◇, 2D), $\Phi_A^n = d(P_A^n - I_A^n)/dt$ (+, 3D; ×, 2D). Dashed line represents the transition time based on the 3D simulation.

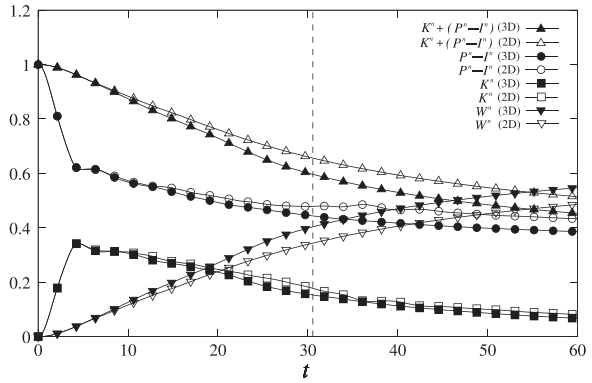

FIG. 14. Energy budget in the system for a supercritical gravity current at $R = 2$ ($S = 0.5$). Symbols: ▲, total mechanical energy $K^n + (P^n - I^n)$ (3D); △, total mechanical energy (2D); ●, potential energy $(P^n - I^n)$ (3D); ○, potential energy (2D); ■, kinetic energy K^n (3D); □, kinetic energy (2D); ▼, dissipated energy W^n (3D); ▽, dissipated energy (2D). Dashed line represents the transition time based on the 3D simulation.

between them for the supercritical case is not as good as for the subcritical case. Please note that for the supercritical case, we choose the energy budget at $R = 2$ ($S = 0.5$) for illustrative purposes. In fact, the discrepancy between the two-dimensional and three-dimensional simulations increases dramatically as the stratification parameter R (S) increases (decreases) for the supercritical gravity currents.

Specifically, in light of the results from the three-dimensional simulation, the potential energy and kinetic energy in the system appear to be overestimated while the dissipated energy is underestimated by the two-dimensional simulation. As also shown in Fig. 15(c), there are two unusual peaks in the dissipation rate, during $5 < t < 17$ and $17 < t < 30$, in the three-dimensional simulation while the two-dimensional simulation tends to underpredict the dissipation rate in the current and in the ambient without apparent peaks. Based on the three-dimensional simulation results, we observe that the lobes and clefts take shape during $5 < t < 17$ and the Kelvin–Helmholtz vortices breakup into three-dimensional structures during $17 < t < 30$. Such an observation explains the difference between the two-dimensional and three-dimensional simulations for the supercritical case but then gives rise to the following question: is the two-dimensional simulation, to which the shallow-water model agrees, able to accurately capture the energy associated with the current and the energy associated with the ambient for the supercritical gravity currents? Interestingly, as shown in Figs. 15(a) and 15(b), the two-dimensional and three-dimensional simulations agree on the kinetic energy associated with the current and the potential energy associated with the ambient. However, the kinetic energy associated with the ambient and the potential energy associated

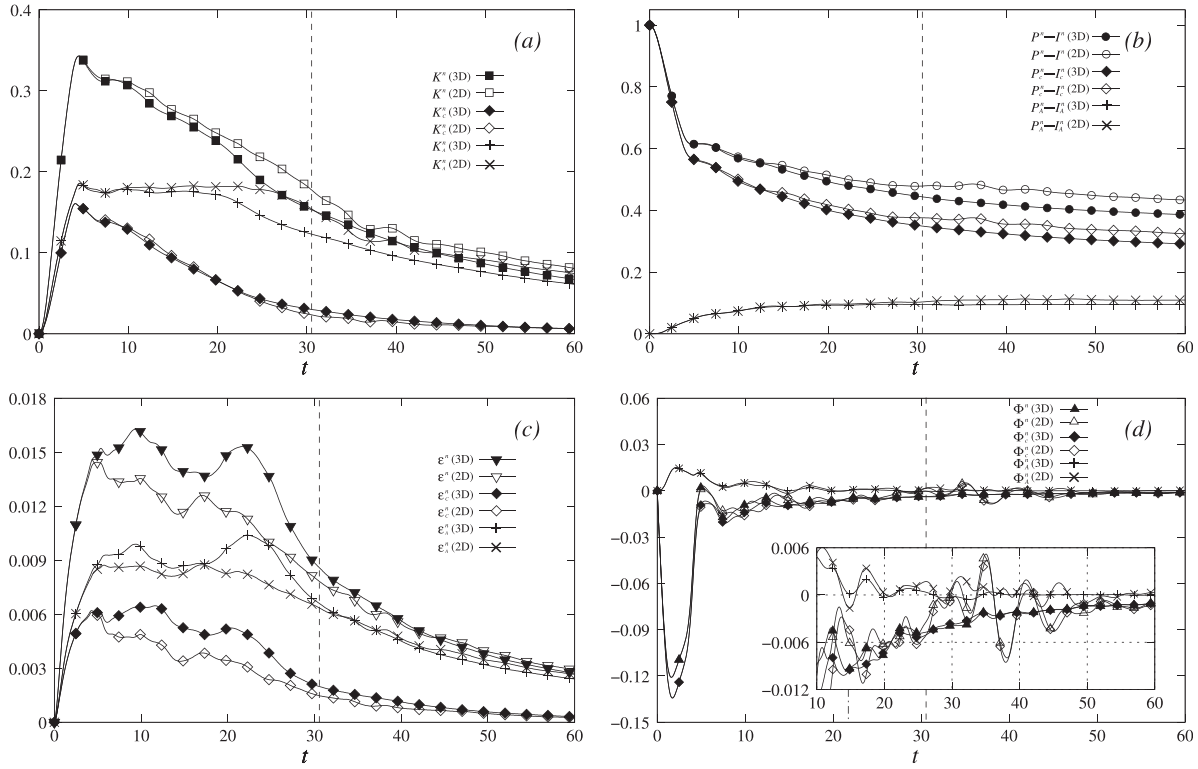

FIG. 15. Energy components in the system for a supercritical gravity current at $R = 2$ ($S = 0.5$). Panel (a) shows K^n (■, 3D; □, 2D), K_C^n (◆, 3D; ◇, 2D), K_A^n (+, 3D; ×, 2D); panel (b) shows $(P^n - I^n)$ (●, 3D; ○, 2D), $(P_C^n - I_C^n)$ (◆, 3D; ◇, 2D), $(P_A^n - I_A^n)$ (+, 3D; ×, 2D); panel (c) shows $\epsilon^n = dW^n/dt$ (▼, 3D; ▽, 2D), $\epsilon_C^n = dW_C^n/dt$ (◆, 3D; ◇, 2D), $\epsilon_A^n = dW_A^n/dt$ (+, 3D; ×, 2D); panel (d) shows $\Phi^n = d(P^n - I^n)/dt$ (▲, 3D; △, 2D), $\Phi_C^n = d(P_C^n - I_C^n)/dt$ (◆, 3D; ◇, 2D), $\Phi_A^n = d(P_A^n - I_A^n)/dt$ (+, 3D; ×, 2D). Dashed line represents the transition time based on the 3D simulation.

with the current are overpredicted by the two-dimensional simulation for the supercritical gravity currents.

Since the dissipation rate in the three-dimensional simulation is higher in the system, including both the current and the ambient, one might ask why the kinetic energy associated with the current can be accurately predicted by the two-dimensional simulation for the supercritical case. Our interpretation is as follows. In the two-dimensional simulation, the Kelvin–Helmholtz vortices, which are preserved as shown in Fig. 7, can withhold the potential energy associated with the current and even create positive buoyancy flux associated with the current at times, as shown in Fig. 15(d). However, in the three-dimensional simulation, the Kelvin–Helmholtz vortices are allowed to breakup and more potential energy associated with the current is released as compensation for the higher dissipation rate. As such, despite the fact that the potential energy associated with the current is overpredicted, the kinetic energy associated with the current is accurately captured by the two-dimensional simulation.

From the energy analysis, we confirm that the stratification in the ambient hinders the decay of the total mechanical energy and enhances the accumulation of potential energy associated with the ambient, as reported previously by Ref. 40. We also show that the stratification in the ambient hinders the decay of potential energy associated with the current and the attainment of kinetic energy in the system. For the subcritical case, the flow is dominated by the internal wave and the two-dimensional simulation accurately captures the kinetic energies and potential energies associated with the current and the ambient. For the supercritical case, the Kelvin–Helmholtz vortices are pronounced in the slumping stage. Although the kinetic energy associated with the current and the potential energy associated with the ambient can be accurately captured, the kinetic energy associated with the ambient and the potential energy associated with the current are overpredicted by the two-dimensional simulation and such a discrepancy increases dramatically as R increases.

D. Partial-depth lock-exchange in a linearly stratified ambient

Limited by our computational resources, currently we are unable to conduct three-dimensional high-resolution simulations for the gravity currents produced from a partial-depth lock-exchange, e.g., $\tilde{H}/\tilde{h}_0 = 2$, in a linearly stratified ambient at sufficiently large Reynolds numbers, e.g., $Re_{h_0} = \sqrt{\tilde{g}_0'\tilde{h}_0}\tilde{h}_0/\tilde{\nu} = 5000$. Here, $\tilde{H}$ is the depth of ambient fluid, $\tilde{h}_0$ is the depth of heavy fluid and the Reynolds number Re_{h_0} is based on the depth of heavy fluid. In full-depth lock-exchange, $\tilde{H}/\tilde{h}_0 = 1$. However, it is possible to conduct two-dimensional simulations for the gravity currents produced from a partial-depth lock-exchange in a linearly stratified ambient for sufficiently large Reynolds numbers. Here, we use two cases to demonstrate that the observations for the subcritical and supercritical cases based on full-depth lock-exchange are still relevant in the partial-depth lock-exchange in a linearly stratified ambient. For both the subcritical ($R = 1.105$) and the supercritical ($R = 2$) cases in this section, we choose $\tilde{H}/\tilde{h}_0 = 2$, $\tilde{L}_0/\tilde{h}_0 = 8/3$ and the Reynolds number based on the depth of heavy fluid as $Re_{h_0} = 5000$. When non-dimensionalized by the depth of heavy fluid, $\tilde{h}_0$, the two-dimensional simulations were performed in the domain $L_{x_1} \times L_{x_3} = 48 \times 2$ and we employed the grid $N_{x_1} \times N_{x_3} = 2816 \times 280$ in the simulations.

Figure 16 shows the passive tracer and the dimensionless density in the ambient of a subcritical gravity current at $R = 1.105$ (left column) and a supercritical gravity current at $R = 2$ (right column) in two-dimensional simulations. It is remarkable that, even with a partial-depth lock release, the Kelvin–Helmholtz vortices are inhibited by the internal waves in the subcritical gravity current and are pronounced in the supercritical gravity current. Our experiments also show consistent trends for the subcritical gravity current at $R = 1.105$ (left column) and supercritical gravity current at $R = 2$ (right column)

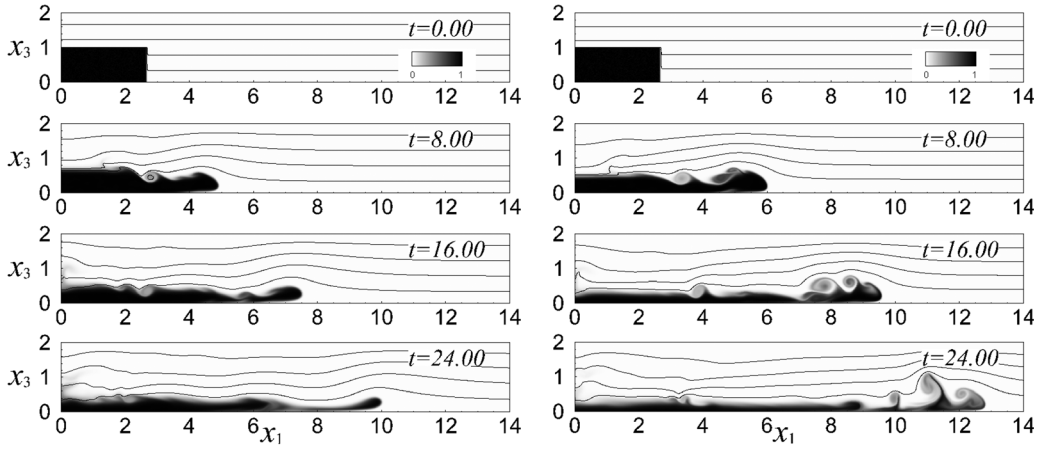

FIG. 16. Sequences of images of a subcritical gravity current ($R = 1.105$) in the two-dimensional simulation (left column) and a supercritical gravity current ($R = 2$) in the two-dimensional simulation (right column). In these two cases, both the subcritical and supercritical gravity currents are produced from a partial-depth lock release, $\tilde{H}/\tilde{h}_0 = 2$, $\tilde{L}_0/\tilde{h}_0 = 8/3$ and the Reynolds number based on the depth of heavy fluid is $Re_{h_0} = 5000$. Distances in the vertical and horizontal directions are normalized by the depth of heavy fluid $\tilde{h}_0$. The black lines in the ambient represent the isopycnals. Time instances are chosen at $t = 0$, 8, 16, and 24 dimensionless units (where time unit is $\tilde{h}_0^{1/2}/\tilde{g}\tilde{r}_0^{1/2}$) for both the subcritical and supercritical cases.

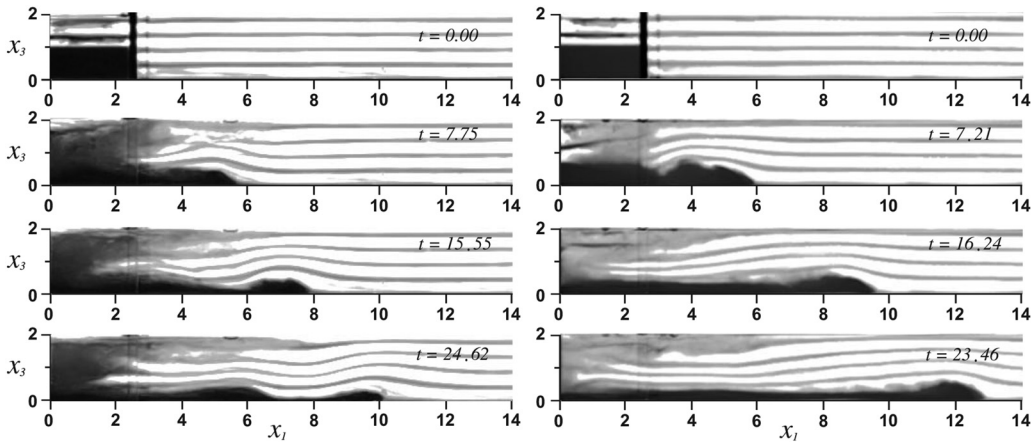

FIG. 17. Sequences of images of a subcritical gravity current ($R = 1.105$) in the experiment (left column) and a supercritical gravity current ($R = 2$) in the experiment (right column). In these two cases, both the subcritical and supercritical gravity currents are produced from a partial-depth lock release, $\tilde{H}/\tilde{h}_0 = 2$, $\tilde{L}_0/\tilde{h}_0 = 8/3$ and the Reynolds number based on the depth of heavy fluid is $Re_{h_0} = 5000$. Distances in the vertical and horizontal directions are normalized by the depth of heavy fluid $\tilde{h}_0$. The black lines in the ambient represent the isopycnals. For the subcritical case (supercritical case), time instances are chosen at $t = 0.00$ (0.00), 7.75 (7.21), 15.55 (16.24), and 24.62 (23.46) dimensionless units (where time unit is $\tilde{h}_0^{1/2}/\tilde{g}'^{1/2}_0$).

in Fig. 17. Based on our two-dimensional and three-dimensional simulations of subcritical and supercritical gravity currents from a full-depth lock release, it is anticipated that, for the partial-depth lock release, the two-dimensional simulation serves as a good surrogate model for the three-dimensional simulation for the subcritical gravity current while, due to the persistence of Kelvin–Helmholtz vortices in the supercritical gravity current, information derived from the two-dimensional simulation must be treated with care for the supercritical case.

V. CONCLUSIONS

Gravity currents, produced from a full-depth lock-exchange setup, propagating at the base of a linearly stratified ambient are reported. Our attention is focused on the slumping stage of propagation. Two-dimensional and three-dimensional high-resolution simulations along with laboratory experiments are conducted to reproduce the quantitative measures of the gravity currents in the slumping stage, including the internal Froude number, transition distance and time, and to provide a detailed energy analysis for the propagation of gravity currents in a linearly stratified ambient.

During the slumping stage, the dynamical pictures between the subcritical case and the supercritical case are qualitatively different. For the subcritical case, the flow is dominated by the internal wave, the Kelvin–Helmholtz vortices are inhibited by the internal wave, and the gravity currents maintain a smooth shape without strong mixing with the ambient fluid. As such, the two-dimensional and three-dimensional simulations agree nicely. For the supercritical case, the current front and the internal wave are locked together and the Kelvin–Helmholtz vortices are pronounced in the slumping stage. The Kelvin–Helmholtz vortices are prone to breakup in the slumping stage and the discrepancy between the two-dimensional and three-dimensional simulations for the supercritical gravity currents increases dramatically as the stratification parameter R increases.

Previously, it was understood that the internal Froude number is a logarithmic function of the stratification parameter R. In this study, we have confirmed that the logarithmic relationship is valid only in the range $1 < R \lesssim 3$ but may fail outside this range. In the limit of large R, the logarithmic relationship diverges from the asymptote Fr_{LR}, given in Eq. (5). We have also shown that the shallow-water model can appropriately describe the internal Froude number throughout the whole range $1 < R \leq 10$ in this study. Previously, the transition distance was understood to be independent of the internal Froude number for the supercritical gravity currents. Our simulation and experimental results indicate that, for the supercritical gravity currents, the transition distance X_{tr} is sensitively dependent on the internal Froude number for the stratification in the ambient in the range $R \lesssim 3$ ($S \gtrsim 1/3$) or $Fr \lesssim 0.72$. For weaker stratification in the ambient in the range $3 \lesssim R \leq 10$ ($1/10 \leq S \lesssim 1/3$) or $0.72 \lesssim Fr \leq 1.45$, the transition distance is weakly dependent on the internal Froude number.

Energy analysis indicates that, for gravity currents propagating into a linearly stratified ambient, the potential energy (with internal energy subtracted) is converted into kinetic energy and then into dissipation but the stratified ambient supports internal waves that can receive energy from the gravity currents. Overall, the stratification in the ambient hinders the decay of the total mechanical energy during the propagation of gravity currents. Specifically, the stratification in the ambient can hinder the release of potential energy associated with the current and the attainment of kinetic energy in the system. For the subcritical case, the two-dimensional and three-dimensional simulations agree nicely in almost all energy components except for the dissipation rate during the time that lobes and clefts take shape. For the supercritical case, the two-dimensional simulation tends to underpredict the dissipation rate in the system during the times that lobes and clefts take shape and the Kelvin–Helmholtz vortices breakup into three-dimensional structures. For the supercritical case, although the kinetic energy associated with the current and the potential energy associated with the ambient can be accurately captured, the kinetic energy

associated with the ambient and the potential energy associated with the current are overpredicted by the two-dimensional simulation and such a discrepancy increases dramatically as the stratification parameter R increases. Information derived from the two-dimensional simulation for the supercritical gravity currents must be treated with care.

The high-resolution simulations reported in this study complement the existing shallow-water formulation and two-dimensional simulations.[39,40] With good physical assumptions and simple mathematical models, the shallow-water formulation has been reported to agree well with the two-dimensional simulations and both the shallow-water formulation and the two-dimensional simulations accurately predict the kinetic energy of the current. The present study is for a full-depth lock-exchange configuration with a rectangular cross section. Future extensions may include the partial-depth release case and an axisymmetric configuration.

ACKNOWLEDGMENTS

The authors wish to thank Professor Marius Ungarish at Technion-Israel Institute of Technology for discussions on the shallow-water model and providing valuable suggestions to improve the manuscript. Computational resources were provided by the Computer and Information Networking Center at National Taiwan University. The research was supported financially by Taiwan Ministry of Science and Technology through Grant Nos. MOST-105-2221-E-002-125-MY2 and MOST-109-2628-E-002-006-MY2.

APPENDIX: OTHER FORMS OF THE BUOYANCY FLUX

In the appendix, we show the connection between the buoyancy flux (18) in our formulation and the informative form defined in Refs. 40 and 2.

In order to manipulate the buoyancy flux into an informative form, Ref. 40 introduces the vertical displacement $\tilde{\eta}$ of a particle of density $\tilde{\rho}_a^*$ in the ambient fluid, from its initial position in the linear density profile. We note that a particle of density $\tilde{\rho}_a^*$ has its initial position in the linear density profile as

$$\frac{\tilde{\rho}_b - \tilde{\rho}_a^*}{\tilde{\rho}_b - \tilde{\rho}_0}\tilde{H},$$

such that a particle of density $\tilde{\rho}_b$ has its initial position at $\tilde{x}_3 = 0$ and a particle of density $\tilde{\rho}_0$ has its initial position at $\tilde{x}_3 = \tilde{H}$. The vertical displacement is defined as

$$\tilde{\eta} = \tilde{x}_3 - \frac{\tilde{\rho}_b - \tilde{\rho}_a^*}{\tilde{\rho}_b - \tilde{\rho}_0}\tilde{H},$$

where $\tilde{x}_3$ is the current position of the particle and $\tilde{\rho}_a^*$ represents the density in the ambient under the influence of internal waves. After some algebra and non-dimensionalized by $\tilde{H}$, the dimensionless vertical displacement is

$$\eta = x_3 - 1 + \frac{\tilde{\rho}_a^* - \tilde{\rho}_0}{\tilde{\rho}_C - \tilde{\rho}_0}\frac{\tilde{\rho}_C - \tilde{\rho}_0}{\tilde{\rho}_b - \tilde{\rho}_0} = x_3 - 1 + \rho_a^* R,$$

where $\rho_a^* = (\tilde{\rho}_a^* - \tilde{\rho}_0)/(\tilde{\rho}_C - \tilde{\rho}_0)$ is the dimensionless density of the ambient under the influence of internal waves. Prior to the release of gravity currents and excitation of internal waves, $\rho_a^* = \rho_a$ in the ambient. Therefore, according to (13), the vertical displacement is $\eta = 0$ prior to the release of gravity currents and excitation of internal waves. Alternatively, we may rewrite the dimensionless density of the ambient in terms of the vertical displacement as

$$\rho_a^* = \frac{\eta}{R} + \frac{1 - x_3}{R} = \frac{\eta}{R} + \rho_a.$$

With the help of the concentration of the passive tracer, we may quantitatively decompose the energies into two parts, i.e., one associated with the gravity currents (denoted by subscript C) and the other associated with the ambient (denoted by subscript A), by the assumption that the density field is related to the concentration of the passive tracer via

$$\rho = C\rho_C + (1 - C)\rho_a^*,$$

where the dimensionless density of the initial heavy fluid is taken as $\rho_C = 1$ and ρ_a^* is the density contribution from the ambient fluid under the influence of internal waves. The buoyancy flux, defined in (18), can be rewritten as

$$\begin{aligned}\Phi &= \int_{\mathcal{V}} \left[C(\rho_c - \rho_a) + (1 - C)\left(\rho_a^* - \rho_a\right)\right] u_3 dV \\ &= \int_{\mathcal{V}} C\left(1 - \frac{1 - x_3}{R}\right) u_3 dV + \int_{\mathcal{V}} (1 - C)\frac{\eta}{R} u_3 dV,\end{aligned}$$

where the first term on the right-hand side represents Φ_C and the second term represents Φ_A. For a non-diffusive simplified system as considered in Ref. 40 the concentration is either 1 or 0 and the domain V is a union of Ω_c (where $C = 1$) and Ω_a (where $C = 0$). For the ambient fluid region Ω_a where $C = 0$, the buoyancy flux associated with the ambient becomes

$$\Phi_A = \int_{\Omega_a} \frac{\eta}{R} u_3 dV = \frac{1}{R}\frac{D}{Dt}\left[\int_{\Omega_a} \frac{1}{2}\eta^2 dV\right],$$

which is consistent with the informative form provided by Refs. 40 and 2.

DATA AVAILABILITY

The data that support the findings of this study are available from the corresponding author upon reasonable request.

REFERENCES

[1] J. Simpson, *Gravity Currents*, 2nd ed. (Cambridge University Press, 1997).
[2] M. Ungarish, *An Introduction to Gravity Currents and Intrusions* (Chapman & Hall/CRC Press, 2009).
[3] J. Shin, S. Dalziel, and P. F. Linden, "Gravity currents produced by lock exchange," J. Fluid Mech. **521**, 1–34 (2004).
[4] M. La Rocca, C. Adduce, G. Sciortino, and A. B. Pinzon, "Experimental and numerical simulation of three-dimensional gravity currents on smooth and rough bottom," Phys. Fluids **20**, 106603 (2008).
[5] M. La Rocca, C. Adduce, V. Lombardi, G. Sciortino, and R. Hinkermann, "Development of a lattice Boltzmann method for two-layered shallow-water flow," Int. J. Numer. Methods Fluids **70**, 1048–1072 (2012).
[6] M. La Rocca, C. Adduce, G. Sciortino, P. A. Bateman, and M. A. Boniforti, "A two-layer shallow water model for 3D gravity currents," J. Hydraul. Res. **50**, 208–217 (2012).
[7] C. Adduce, G. Sciortino, and S. Proietti, "Gravity currents produced by lock-exchanges: xperiments and simulations with a two layer shallow-water model with entrainment," J. Hydraul. Eng. **138**, 111–121 (2012).

[8]A. Dai, "Experiments on gravity currents propagating on different bottom slopes," J. Fluid Mech. **731**, 117–141 (2013).
[9]V. Lombardi, C. Adduce, G. Sciortino, and M. La Rocca, "Gravity currents flowing upslope: laboratory experiments and shallow-water simulations," Phys. Fluids **27**, 016602 (2015).
[10]L. Ottolenghi, C. Adduce, R. Inghilesi, V. Armenio, and F. Roman, "Entrainment and mixing in unsteady gravity currents," J. Hydraul. Res. **54**, 541–557 (2016).
[11]L. Ottolenghi, C. Adduce, R. Inghilesi, F. Roman, and V. Armenio, "Mixing in lock-release gravity currents propagating up a slope," Phys. Fluids **28**, 056604 (2016).
[12]L. Ottolenghi, C. Adduce, F. Roman, and V. Armenio, "Analysis of the flow in gravity currents propagating up a slope," Ocean Model. **115**, 1–13 (2017).
[13]J. Zhou, C. Cenedese, T. Williams, M. Ball, S. K. Venayagamoorthy, and R. I. Nokes, "On the propagation of gravity currents over and through a submerged array of circular cylinders," J. Fluid Mech. **831**, 394–417 (2017).
[14]R. Inghilesi, C. Adduce, V. Lombardi, F. Roman, and V. Armenio, "Axisymmetric three-dimensional gravity currents generated by lock exchange," J. Fluid Mech. **851**, 507–544 (2018).
[15]F. Kyrousi, A. Leonardi, F. Roman, V. Armenio, F. Zanello, J. Zordan, C. Juez, and L. Falcomer, "Large Eddy Simulations of sediment entrainment induced by a lock-exchange gravity current," Adv. Water Resour. **114**, 102–118 (2018).
[16]V. Lombardi, C. Adduce, and M. La Rocca, "Unconfined lock-exchange gravity currents with variable lock width: laboratory experiments and shallow-water simulations," J. Hydraul. Res. **56**, 399–411 (2018).
[17]L. Ottolenghi, P. Prestininzi, A. Montessori, C. Adduce, and M. La Rocca, "Lattice Boltzmann simulations of gravity currents," Eur. J. Mech. B/Fluids **67**, 125–136 (2018).
[18]J. Pelmard, S. Norris, and H. Friedrich, "LES grid resolution requirements for the modelling of gravity currents," Compt. Fluids **174**, 256–270 (2018).
[19]A. Martin, M. E. Negretti, and E. J. Hopfinger, "Development of gravity currents on slopes under different interfacial instability conditions," J. Fluid Mech. **880**, 180–208 (2019).
[20]M. C. De Falco, L. Ottolenghi, and C. Adduce, "Dynamics of gravity currents flowing up a slope and implications for entrainment," J. Hydraul. Eng. **146**, 04020011 (2020).
[21]J. Pelmard, S. Norris, and H. Friedrich, "Statistical characterisation of turbulence for an unsteady gravity current," J. Fluid Mech. **901**, A7 (2020).
[22]M. C. De Falco, C. Adduce, M. E. Negretti, and E. J. Hopfinger, "On the dynamics of quasi-steady gravity currents flowing up a slope," Adv. Water Resour. **147**, 103791 (2021).
[23]J. W. Rottman and J. E. Simpson, "Gravity currents produced by instantaneous releases of a heavy fluid in a rectangular channel," J. Fluid Mech. **135**, 95–110 (1983).
[24]M. Cantero, J. Lee, S. Balachandar, and M. Garcia, "On the front velocity of gravity currents," J. Fluid Mech. **586**, 1–39 (2007).
[25]J. Wu, "Mixed region collapse with internal wave generation in a density-stratified medium," J. Fluid Mech. **35**, 531–544 (1969).
[26]A. H. Schooley and B. A. Hughes, "An experimental and theoretical study of internal waves generated by the collapse of a two-dimensional mixed region in a density gradient," J. Fluid Mech. **51**, 159–175 (1972).
[27]R. Amen and T. Maxworthy, "The gravitational collapse of a mixed region into a linearly stratified fluid," J. Fluid Mech. **96**, 65–80 (1980).
[28]M. R. Flynn and B. R. Sutherland, "Intrusive gravity currents and internal gravity wave generation in stratified fluid," J. Fluid Mech. **514**, 355–383 (2004).
[29]M. Ungarish, "Intrusive gravity currents in a stratified ambient: Shallow-water theory and numerical results," J. Fluid Mech. **535**, 287–323 (2005).
[30]M. R. Flynn and P. F. Linden, "Intrusive gravity currents," J. Fluid Mech. **568**, 193–202 (2006).
[31]G. La Forgia, L. Ottolenghi, C. Adduce, and F. Falcini, "Intrusions and solitons: Propagation and collision dynamics," Phys. Fluids **32**, 076605 (2020).
[32]L. Ottolenghi, C. Adduce, F. Roman, and G. La Forgia, "Large Eddy simulations of solitons colliding with intrusions," Phys. Fluids **32**, 096606 (2020).
[33]T. Maxworthy, J. Leilich, J. E. Simpson, and E. H. Meiburg, "The propagation of a gravity current into a linearly stratified fluid," J. Fluid Mech. **453**, 371–394 (2002).
[34]M. Ungarish and T. Zemach, "On the slumping of high Reynolds number gravity currents in two-dimensional and axisymmetric configurations," Eur. J. Mech. B/Fluids **24**, 71–90 (2005).
[35]M. Ungarish, "Dam-break release of a gravity current in a stratified ambient," Eur. J. Mech. B/Fluids **24**, 642–658 (2005).
[36]B. L. White and K. R. Helfrich, "Gravity currents and internal waves in a stratified fluid," J. Fluid Mech. **616**, 327–356 (2008).
[37]M. Ungarish, "On gravity currents in a linearly stratified ambient: a generalization of Benjamin's steady-state propagation results," J. Fluid Mech. **548**, 49–68 (2006).
[38]V. K. Birman, E. Meiburg, and M. Ungarish, "On gravity currents in stratified ambients," Phys. Fluids **19**, 086602 (2007).
[39]M. Ungarish and H. E. Huppert, "On gravity currents propagating at the base of a stratified ambient," J. Fluid Mech. **458**, 283–307 (2002).
[40]M. Ungarish and H. E. Huppert, "Energy balances for propagating gravity currents: homogeneous and stratified ambients," J. Fluid Mech. **565**, 363–380 (2006).
[41]C. Härtel, E. Meiburg, and F. Necker, "Analysis and direct numerical simulation of the flow at a gravity-current head. Part 1. Flow topology and front speed for slip and no-slip boundaries," J. Fluid Mech. **418**, 189–212 (2000).
[42]F. Necker, C. Härtel, L. Kleiser, and E. Meiburg, "Mixing and dissipation in particle-driven gravity currents," J. Fluid Mech. **545**, 339–372 (2005).
[43]T. Bonometti and S. Balachandar, "Effect of Schmidt number on the structure and propagation of density currents," Theor. Comput. Fluid Dyn. **22**, 341–361 (2008).
[44]R. Peyret, *Spectral Methods for Non compressible Viscous Low* (Springer-Verlag, New York, 2002).
[45]T. Maxworthy, "The dynamics of double-diffusive gravity currents," J. Fluid Mech. **128**, 259–282 (1983).
[46]G. Sciortino, C. Adduce, and V. Lombardi, "A new front condition for non-Boussinesq gravity currents," J. Hydraul. Res. **56**, 517–525 (2018).
[47]J. H. Williamson, "Low-storage Runge-Kutta schemes," J. Comput. Phys. **35**, 48–56 (1980).
[48]D. Durran, *Numerical Methods for Wave Equations in Geophysical Fluid Dynamics* (Springer, 1999).
[49]A. Dai, "High-resolution simulations of downslope gravity currents in the acceleration phase," Phys. Fluids **27**, 076602 (2015).
[50]A. Dai and Y.-L. Huang, "High-resolution simulations of non-Boussinesq downslope gravity currents in the acceleration phase," Phys. Fluids **28**, 026602 (2016).
[51]A. Dai and C.-S. Wu, "High-resolution simulations of cylindrical gravity currents in a rotating system," J. Fluid Mech. **806**, 71–101 (2016).
[52]C. Härtel, L. K. M. Michaud, and C. Stein, "A direct numerical simulation approach to the study of intrusion fronts," J. Eng. Math. **32**, 103–120 (1997).
[53]V. K. Birman, J. E. Martin, and E. Meiburg, "The non-boussinesq lock-exchange problem. Part 2. High-resolution simulations," J. Fluid Mech. **537**, 125–144 (2005).
[54]G. Oster, "Density gradients," Sci. Am. **213**, 70–76 (1965).
[55]K. B. Winters, P. N. Lombard, J. J. Riley, and E. A. D'Asaro, "Available potential energy and mixing in density-stratified fluids," J. Fluid Mech. **289**, 115–128 (1995).